
On What We Can Learn from Low-Resolution Data

Theresa Dahl Frehr^{1*} Niels Henrik Pontoppidan² Hiba Nassar¹ Tommy Sonne Alstrøm¹

¹Technical University of Denmark ²Eriksholm Research Center
{tdafr, hibna, tsal}@dtu.dk npon@eriksholm.com

Abstract

Artificial intelligence systems typically rely on large, centrally collected datasets, a premise that does not hold in many real-world domains such as healthcare and public institutions. In these settings, data sharing is often constrained by storage, privacy, or resource limitations. For example, small wearable devices may lack the bandwidth or energy capacity needed to store and transmit high-resolution data, leading to aggregation during data collection and thus a loss of information. As a result, datasets collected from different sources may consist of a mixture of high- and low-resolution samples. Despite the prevalence of this setting, it remains unclear how informative low-resolution data is when models are ultimately evaluated on high-resolution inputs. We provide a theoretical analysis based on the Kullback–Leibler divergence that characterises how the influence of a datapoint changes with resolution, and derive bounds that relate the relative contribution of high- and low-resolution observations to the information lost under downsampling. To support this analysis, we empirically demonstrate, using both a vision transformer and a convolutional neural network, that adding low-resolution data to the training set consistently improves performance when high-resolution data is scarce.

1 Introduction

Large-scale artificial intelligence (AI) systems rely on massive datasets, substantial storage, computation, and data-transfer resources. In many real-world settings, however, such as healthcare systems, public institutions, and distributed data ecosystems, these resources are limited, and sharing raw data across institutions is often constrained by privacy, regulatory, security, or storage requirements [El Mestari et al., 2024, Zerka et al., 2020, Fang et al., 2024, Pati et al., 2024]. This makes it difficult to assemble the large centralised datasets on which modern AI systems depend.

A representative example arises in wearable devices, such as smart watches and hearing aids, which continuously collect data in everyday use [Christensen et al., 2021, Pati et al., 2024, Wani and Can, 2025]. Privacy constraints, limited bandwidth, and energy resources prevent storage and transmission of raw high-resolution data. Instead, the devices only transmit feature-based representations or temporally downsampled summaries [Pontoppidan et al., 2018, Zhao and Fan, 2024]. For example, a wearable device may monitor movement or acoustic conditions continuously, but if only a coarse temporal summary is transmitted, short-lived changes and other fine-grained patterns in the original signal are no longer retained, yielding the mixed-resolution setting illustrated in Figure 1. As a result, datasets collected from multiple sources may contain a mixture of high- and low-resolution datapoints. Despite the prevalence of such settings, the question of how much task-relevant information is retained in low-resolution data remains largely unexplored. Existing work on low-resolution learning has primarily focused on super-resolution or on improving robustness and efficiency at inference time, rather than understanding the role of low-resolution data during training under storage and privacy constraints [Zangeneh et al., 2020, Ge et al., 2019].

*This work was supported by the William Demant Fonden (24-5326)

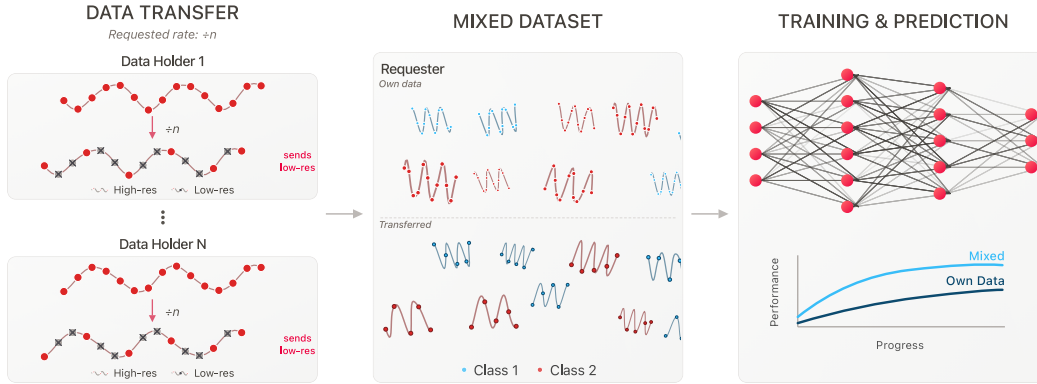


Figure 1: Illustration of the formation of a mixed-resolution dataset. A central party (the requester) possesses a limited amount of high-resolution data and requests additional data from multiple external data holders. Due to bandwidth and storage constraints, the exchanged data are provided at a lower resolution agreed upon by all parties. The resulting dataset consists of the requester’s high-resolution samples combined with low-resolution data from external sources, on which model training is subsequently performed.

In this work, we treat low-resolution observations not as a nuisance to be corrected, but as a deliberate design choice motivated by practical constraints. We consider a setting in which the training data comprise both high- and low-resolution datapoints. Each datapoint is assumed to be generated at a single resolution and is therefore only available in either high- or low-resolution forms. We investigate how much task-relevant information is preserved under downsampling, and to what extent low-resolution data contribute to models evaluated on high-resolution inputs. This is carried out by a theoretical analysis studying how the contribution of a datapoint would differ if it were realised at a different resolution. We support this analysis empirically by considering two model types: a Vision Transformer (ViT) and a Convolutional Neural Network (CNN). While both architectures can accommodate inputs of varying spatial resolution, they do so in fundamentally different ways. ViTs accommodate changing input resolution through patch tokenisation and positional embedding (PE) interpolation, whereas CNNs require an adaptive pooling prior to classification. Comparing the two allows us to assess how architectural inductive biases interact with the information lost under downsampling.

Our main contributions are

1. We provide a theoretical characterisation of the relative influence of high- and low-resolution versions of a datapoint on the model parameter distribution, and derive bounds that relate this influence to the information missing from the lower-resolution representation.
2. Through experiments on standard benchmarks, we demonstrate that low-resolution data can improve performance on high-resolution evaluation tasks when high-resolution data is scarce.

2 Related Work

Prior methods for learning across resolutions typically either require access to samples at multiple resolutions, perform testing purely in low-resolution regimes, or focus on robustness to resolution shifts. In contrast, we study mixed-resolution training without paired observations, focusing on the performance on high-resolution inputs at test time.

Super-Resolution and Cross-Resolution Learning Super-resolution methods aim to reconstruct high-resolution images from low-resolution inputs [Saharia et al., 2022, Zamir et al., 2020, Wang et al., 2015, Hui et al., 2019] and are sometimes used as a preprocessing step to improve downstream performance [Koziarski and Cyganek, 2018, Wang et al., 2016]. While effective in certain regimes, such approaches are misaligned with storage- and resource-constrained settings.

Cross-resolution learning frameworks typically rely on explicit alignment between high- and low-resolution representations. For example, [Wang et al., 2016] combine super-resolution pretraining with cross-resolution feature transfer and partially shared architectures, while [Peng et al., 2016] employ a staged fine-to-coarse training pipeline requiring paired high- and low-resolution samples. Such assumptions are impractical when low-resolution data originates from external sources. Additionally, upscaling low-resolution samples to fit standard CNN architectures is storage-inefficient. While [Kozierski and Cyganek, 2018] show that accuracy degrades with decreasing resolution, they do not consider training across multiple resolutions.

Low-Resolution Recognition Low-resolution data features prominently in surveillance applications, making low-resolution face recognition an active research area. Prior work includes multidimensional scaling [Mudunuri and Biswas, 2016, Yang et al., 2018], discriminative subspace alignment with multiple CNNs [Lu et al., 2018, Zangeneh et al., 2020], simultaneous discriminant analysis [Chu et al., 2017], and knowledge distillation [Ge et al., 2019]. While effective under cross-resolution mismatch, these methods focus on inference in low-resolution regimes rather than exploiting low-resolution data to improve high-resolution performance.

Learning from Compressed Representations A smaller body of work considers learning directly from compressed or downsampled inputs. RandNet [Chang et al., 2019] enables supervised learning from low-resolution data and connects to dictionary learning. Earlier theoretical work by [Fabisch et al., 2013] shows that representing a network’s weights using a lower-dimensional parameterisation is mathematically equivalent to projecting its inputs into a lower-dimensional space. However, these approaches do not address whether training on mixed resolutions improves generalisation to high-resolution inputs.

Multi-Resolution Training of Transformers Multi-resolution training has been explored in time-series transformers [Chen et al., 2024, Wang et al., 2024, Zhang et al., 2024], where varying patch sizes capture patterns at different temporal scales. In computer vision, ResFormer [Tian et al., 2023] enforces scale consistency by replicating batches across resolutions in conjunction with a scale consistency loss, while ViTAR [Fan et al., 2024] introduces fuzzy PEs to improve robustness to resolution shifts. Although these methods improve cross-resolution robustness, they do not examine the benefit of incorporating low-resolution data during training, and batch replication is inefficient in resource-constrained settings.

CNNs and Vision Transformers CNNs [LeCun et al., 1989] process images through convolutional layers that apply learnable local filters across spatial neighbourhoods. This hierarchical structure enables the extraction of progressively more complex features, from edges and textures in early layers to high-level semantic representations in deeper layers. Weight sharing and translation equivariance provide strong inductive biases. In contrast, ViTs [Dosovitskiy et al., 2021] treat images as sequences of fixed-size patches processed by Transformer encoder layers with PEs. Self-attention enables global interactions across patches from the first layer onward, although ViTs lack the locality and equivariance biases of CNNs.

3 Problem Formulation

We study supervised learning in a setting where training data is not available at a single common resolution, while models are ultimately evaluated on high-resolution inputs only. Let $\mathcal{S}(\mathcal{D}) = \{S(d) : d \in \mathcal{D}\}$ be a stochastic process defined on a continuous domain $\mathcal{D} = [0, M]$, and let a datapoint \mathbf{x} be a finite-dimensional representation of a realisation of the process \mathcal{S} . Let s and t denote two integer sampling rates where $s > t$. A high-resolution datapoint $\mathbf{x}_h \in \mathbb{R}^s$ is represented by s coefficients, while a low-resolution datapoint $\tilde{\mathbf{x}}_l \in \mathbb{R}^t$ is represented by t coefficients. To compare the two in a common space, \mathbb{R}^s , we introduce an upsampling operator $f : \mathbb{R}^t \rightarrow \mathbb{R}^s$ and define $\mathbf{x}_l := f(\tilde{\mathbf{x}}_l) \in \mathbb{R}^s$. The operator preserves the alignment of the coefficients, such that, in this representation, \mathbf{x}_h admits the decomposition: $\mathbf{x}_h = \mathbf{x}_l + \mathbf{x}_r$. Here $\mathbf{x}_r \in \mathbb{R}^s$ denotes the residual component, i.e. the information present in the high-resolution representation but absent in the low-resolution one.

Let $\mathcal{X} = \{\mathbf{x}_1, \mathbf{x}_2, \dots, \mathbf{x}_N\}$ be a training dataset consisting of a mixture of high- and low-resolution datapoints, where each datapoint is observed at exactly one resolution. We consider a parametric model with parameters $\theta \in \Theta$ trained using a loss function $\ell(\theta, \mathbf{x})$. For notational simplicity, we

write $\ell(\boldsymbol{\theta}, \mathbf{x})$ as shorthand for $\ell(\boldsymbol{\theta}; \mathbf{x}, y)$, i.e. the target y is suppressed whenever it is fixed and unambiguous. All derivatives with respect to the input are taken with respect to the observation \mathbf{x} , not the target y . For a new datapoint, \mathbf{x}_i , we define its influence as the change in the parameter distribution induced by its inclusion:

$$\text{KL}_i := \text{KL}(p(\boldsymbol{\theta} \mid \mathcal{X}) \parallel p(\boldsymbol{\theta} \mid \mathcal{X} \cup \{\mathbf{x}_i\})), \quad (1)$$

where KL denotes the Kullback-Leibler divergence [Kullback and Leibler, 1951]. In the following analysis, \mathbf{x}_h and \mathbf{x}_l are treated as fixed realisations of the same underlying datapoint at different resolutions. Consequently, randomness arises from $\boldsymbol{\theta}$ only.

Our central question is how the influence of a datapoint changes when it is observed at a different resolution. We characterise this difference by relating KL_h and KL_l to the residual component \mathbf{x}_r , which represents the information present in \mathbf{x}_h , but absent from \mathbf{x}_l . In contrast to prior work, we do not assume access to paired high- and low-resolution samples, nor do we require high-resolution reconstruction.

4 Theoretical Analysis

In this section, we theoretically analyse the effect of adding a high- versus a low-resolution datapoint to the training set. Following Sablayrolles et al. [2019] and [Dong et al., 2022] we model the parameters $\boldsymbol{\theta}$ as a random variable whose distribution depends on the training set \mathcal{X} .

Assumption 1 (Gibbs Distribution) *Given a dataset \mathcal{X} and a loss function $\ell(\boldsymbol{\theta}, \mathbf{x})$, the distribution of model parameters, $\boldsymbol{\theta}$, is given by*

$$p(\boldsymbol{\theta} \mid \mathcal{X}) = \frac{1}{Z(\mathcal{X})} \exp\left(-\frac{1}{\gamma} \sum_{\mathbf{x} \in \mathcal{X}} \ell(\boldsymbol{\theta}, \mathbf{x})\right), \quad (2)$$

where the partition function $Z(\mathcal{X}) = \int_{\Theta} \exp\left(-\frac{1}{\gamma} \sum_{\mathbf{x} \in \mathcal{X}} \ell(\boldsymbol{\theta}, \mathbf{x})\right) d\boldsymbol{\theta}$ is assumed to be finite.

Without loss of generality we set the temperature parameter $\gamma = 1$ for the remainder of the paper. To facilitate the analysis, we impose regularity conditions on the loss function.

Assumption 2 (Properties of Loss Function) *The loss function $\ell(\boldsymbol{\theta}, \mathbf{x})$ is assumed to be twice continuously differentiable in \mathbf{x} and locally linear². Moreover, there exist constants $C_1, C_2 < \infty$ such that*

$$\mathbb{E}_{q(\boldsymbol{\theta})} [|\ell(\boldsymbol{\theta}, \mathbf{x})|] \leq C_1, \quad \mathbb{E}_{q(\boldsymbol{\theta})} [\ell(\boldsymbol{\theta}, \mathbf{x})^2] \leq C_2, \quad \mathbf{x} \in \{\mathbf{x}_h, \mathbf{x}_l\}, \quad q(\boldsymbol{\theta}) \in \{p(\boldsymbol{\theta} \mid \mathcal{X}), p(\boldsymbol{\theta} \mid \mathcal{X} \cup \{\mathbf{x}_l\})\}, \quad (3)$$

hence, under the relevant posterior, the first and second moment of $\ell(\boldsymbol{\theta}, \mathbf{x}_h)$ and $\ell(\boldsymbol{\theta}, \mathbf{x}_l)$ are bounded.

We will now state the first result. The ratio of KL-divergences for including a point at either high- or low-resolution admits a closed-form expression as given by the following proposition (Proof in Appendix A.2).

Proposition 3 (Exact KL-divergence) *Under Assumption 1 the ratio of KL-divergences is given by:*

$$\frac{\text{KL}_h}{\text{KL}_l} = \frac{\log(\mathbb{E}_{\boldsymbol{\theta} \mid \mathcal{X}}[\exp(-\ell(\boldsymbol{\theta}, \mathbf{x}_h))] + \mathbb{E}_{\boldsymbol{\theta} \mid \mathcal{X}}[\ell(\boldsymbol{\theta}, \mathbf{x}_h)])}{\log(\mathbb{E}_{\boldsymbol{\theta} \mid \mathcal{X}}[\exp(-\ell(\boldsymbol{\theta}, \mathbf{x}_l))] + \mathbb{E}_{\boldsymbol{\theta} \mid \mathcal{X}}[\ell(\boldsymbol{\theta}, \mathbf{x}_l)])}. \quad (4)$$

Proposition 3 characterises datapoint influence through the behaviour of the loss under the posterior distribution over parameters. A ratio above 1 means that the high-resolution point exerts a larger influence than its low-resolution counterpart, while a ratio of 1 means there is no gain in the extra information in the high-resolution representation.

Recognizing the cumulant generating function [Kendall, 1943] in eq. (4) reveals that datapoint influence is directly affected by higher-order moments. Approximating it to second order shows that the leading effect is governed by the variance of the loss as seen in the following proposition (proof in Appendix A.3).

²Locally linear is defined explicitly in definition (A2) in Appendix A.

Proposition 4 (Variance Approximation) *Under assumptions 1 and 2, the ratio of KL-divergences admits the second-order approximation*

$$\frac{\text{KL}_h}{\text{KL}_l} \approx \frac{\text{Var}_{\theta|\mathcal{X}}[\ell(\boldsymbol{\theta}, \mathbf{x}_h)]}{\text{Var}_{\theta|\mathcal{X}}[\ell(\boldsymbol{\theta}, \mathbf{x}_l)]}. \quad (5)$$

This result provides an interpretable measure of datapoint influence. Intuitively, a datapoint must exert a larger influence on parameter distribution if the loss changes greatly across different realisations. The following proposition provides bounds of the ratio of KL-divergences, showing that the relative influence of a high-resolution datapoint is controlled by the residual component \mathbf{x}_r (proof is found in Appendix A.4).

Proposition 5 (Ratio of KL-divergence) *Under assumptions 1 and 2, the ratio of KL-divergence satisfies the approximate bounds*

$$\left(1 - \sqrt{\frac{\|\mathbf{x}_r\|_{\Sigma_g}^2}{\sigma_l^2}}\right)^2 \leq \frac{\text{KL}_h}{\text{KL}_l} \leq \left(1 + \sqrt{\frac{\|\mathbf{x}_r\|_{\Sigma_g}^2}{\sigma_l^2}}\right)^2, \quad (6)$$

where $\sigma_l^2 = \text{Var}_{\theta|\mathcal{X}}[\ell(\boldsymbol{\theta}, \mathbf{x}_l)]$, $\mathbf{g} = \nabla_{\mathbf{x}}\ell(\boldsymbol{\theta}, \mathbf{x})|_{\mathbf{x}=\mathbf{x}_l}$ and Σ_g the covariance matrix of \mathbf{g} under $p(\boldsymbol{\theta} | \mathcal{X})$.

While Proposition 5 characterises the relative influence of high- and low-resolution representations, it is also useful to quantify their absolute difference. Proposition 6 provides bounds on the difference between the two KL-divergences, which measures the additional contribution of the high-resolution representation.

Proposition 6 (Difference in KL-divergence) *Under assumptions 1 and 2 the difference in KL-divergences admits the approximate bounds,*

$$\frac{1}{2}\|\mathbf{x}_r\|_{\Sigma_g}^2 - \zeta\|\mathbf{x}_r\|_{\Sigma_l} \leq \text{KL}_h - \text{KL}_l \leq \frac{1}{2}\|\mathbf{x}_r\|_{\Sigma_l}^2 + \zeta\|\mathbf{x}_r\|_{\Sigma_g}, \quad (7)$$

where $\zeta = \sqrt{\text{Var}_{\theta|\mathcal{X} \cup \{\mathbf{x}_l\}}[\exp(\ell(\boldsymbol{\theta}, \mathbf{x}_l))]/\mathbb{E}_{\theta|\mathcal{X} \cup \{\mathbf{x}_l\}}[\exp(\ell(\boldsymbol{\theta}, \mathbf{x}_l))]}$, $\mathbf{g} = \nabla_{\mathbf{x}}\ell(\boldsymbol{\theta}, \mathbf{x})|_{\mathbf{x}=\mathbf{x}_l}$ and Σ_g^l is the covariance matrix of \mathbf{g} under $p(\boldsymbol{\theta} | \mathcal{X} \cup \{\mathbf{x}_l\})$.

Taken together, propositions 5 and 6 characterise both the relative and absolute benefit of including a datapoint at higher resolution. Proposition 5 shows that the relative gain depends on the directional residual norm $\|\mathbf{x}_r\|_{\Sigma_g}$, normalised by σ_l^2 . In particular, when σ_l^2 is large, the low-resolution datapoint already exerts large influence on the parameter distribution, making the benefit of the extra coefficients smaller. Proposition 6 complements this with a correction term governed by ζ . Together, these results show that the utility of low-resolution data depends not only on how much information is discarded during downsampling, but also on how sensitive the loss is to that missing information.

Importantly, the analysis does not impose any restriction on the resolutions present in \mathcal{X} , which may contain datapoints observed at multiple different resolutions; the propositions quantify how the contribution of a datapoint changes when it is observed at a higher resolution. More generally, the results do not depend on the particular choice of the t coefficients defining \mathbf{x}_l , assuming that the upsampling operator preserves alignment between coefficients in \mathbf{x}_l and \mathbf{x}_h . Under this view, the same analysis extends beyond spatial or temporal resolution: \mathbf{x}_l may equivalently represent a partial feature observation, in which case the residual component \mathbf{x}_r corresponds to the missing features.

The bounds in propositions 5 and 6 are obtained by controlling covariance terms via the Cauchy-Schwarz inequality [Gut, 2013], which yields worst-case bounds. If these covariance terms are known to be non-negative, the lower bounds can be improved. The resulting tighter bounds are stated in Corollary 7 with proofs in Appendix B.2.

Corollary 7 (Tighter Lower Bounds) *Under Assumptions 1 and 2, suppose additionally that $\text{Cov}_{\theta|\mathcal{X}}[\mathbf{g}^\top \mathbf{x}_r, \ell(\boldsymbol{\theta}, \mathbf{x}_l)] \geq 0$ and $\text{Cov}_{\theta|\mathcal{X} \cup \{\mathbf{x}_l\}}[\mathbf{g}^\top \mathbf{x}_r, \exp(\ell(\boldsymbol{\theta}, \mathbf{x}_l))] \geq 0$. Then propositions 5 and 6 admit the tighter lower bounds*

$$1 + \frac{\|\mathbf{x}_r\|_{\Sigma_g}^2}{\sigma_l^2} \leq \frac{\text{KL}_h}{\text{KL}_l}, \quad \frac{1}{2}\|\mathbf{x}_r\|_{\Sigma_l}^2 \leq \text{KL}_h - \text{KL}_l, \quad (8)$$

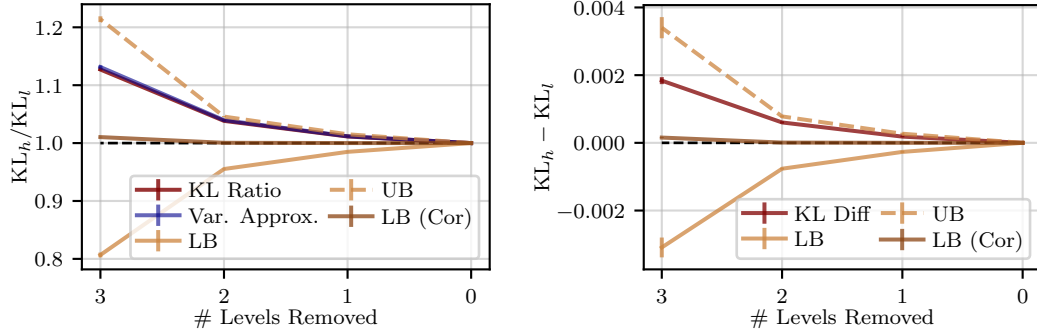


Figure 2: Simulation of bounds as a function of progressively removed high-frequency content. Error bars denote ± 5 times the standard deviation. As more high-frequency components are removed, the influence of low-resolution datapoints decreases, validating the theoretical predictions. UB = upper bound, LB = lower bound. Cor denotes bounds from Corollary 7. **Left:** True KL-divergence ratio, variance-based approximation from Proposition 4, the bounds from Proposition 5 and the tighter ratio lower bound from Corollary 7 **Right:** True KL-divergence difference, the bounds from Proposition 6, and the tighter difference lower bound from Corollary 7.

where $\sigma_l^2 = \text{Var}_{\theta|\mathcal{X}}[\ell(\theta, \mathbf{x}_l)]$, $\mathbf{g} = \nabla_{\mathbf{x}} \ell(\theta, \mathbf{x})|_{\mathbf{x}=\mathbf{x}_l}$, and $\Sigma_{\mathbf{g}}$ and $\Sigma_{\mathbf{g}}^l$ are the covariance matrix of \mathbf{g} under $p(\theta | \mathcal{X})$ and $p(\theta | \mathcal{X} \cup \{\mathbf{x}_l\})$ respectively.

Under these non-negative covariance assumptions, the lower bound on the KL-ratio is strictly above 1, and the lower bound on the KL-difference is strictly positive whenever $\mathbf{x}_r \neq \mathbf{0}$. Thus, in this regime, the high-resolution datapoint is guaranteed to be more influential than its low-resolution counterpart. The proofs of Propositions 5 and 6 rely on a first-order Taylor expansion. Appendix B derives corresponding bounds using a second-order expansion and shows through simulations that this refinement does not produce better bounds.

4.1 Simulations of Theoretical Results

To validate the theoretical results, we conduct a series of simulations. For this, we need a dataset where a high-resolution datapoint fulfils the decomposition $\mathbf{x}_h = \mathbf{x}_l + \mathbf{x}_r$. To construct such a dataset, the first 100 images from each of the first two classes of CIFAR-10 are extracted. For each of the datapoints a scalogram using the Discrete Wavelet Transform (DWT) is computed with three levels using the db2 mother wavelet [Mallat, 2009]. To create different degrees of downsampled data, the bands in the scalogram containing the highest frequencies are progressively set to zero. The final datapoint, \mathbf{x}_l , is restored using the inverse DWT and projected to a 10-dimensional vector using PCA. For more details on how this ensures that $\mathbf{x}_h = \mathbf{x}_l + \mathbf{x}_r$ we refer to Appendix C.

A neural network consisting of four linear layers with ReLU activations is then trained to distinguish between the two classes. We compute the true KL-divergences using the expression in Proposition 3, assess the approximation in Proposition 4, and compute the two bounds from propositions 5 and 6 as well as the tighter bounds in Corollary 7. Results are depicted in Figure 2 and generated by training 10,000 models repeated over five random seeds. The black dashed line in the left panel denotes a fraction of 1, and in the right panel it denotes a difference of 0. The x -axis denotes the number of levels/frequency bands that have been removed where 0 is no removal. Exact KL-divergence values and their corresponding bounds can be found in Appendix D.

The variance approximation captures the overall behaviour of the KL-ratio. For both the KL-ratio and KL-difference, the lower and upper bounds become looser as the magnitude of the residual component increases. The tighter bounds introduced in Corollary 7 are indeed tighter which is consistent with the corresponding covariance terms being non-negative. A more detailed analysis of the accuracy of the variance approximation and of the tightness of the bounds as a function of model size and input dimension is provided in Appendix E.

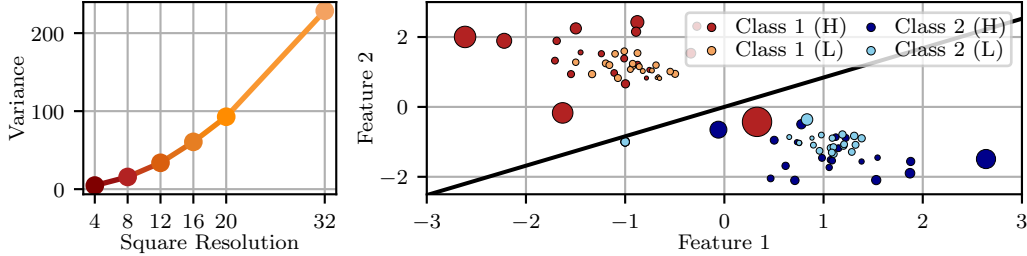


Figure 3: **Left:** Variance of low-dimensional representations as a function of image resolution. Computed from PCA projections of progressively downsampled images from CIFAR10. **Right:** Synthetic two-class data separated using linear discriminant analysis. Marker size given by the magnitude of the change in model parameters when including a datapoint in the training set. The black line is the decision boundary given by training on all points.

4.2 Toy Example

To illustrate when a high-resolution datapoint can be more informative than its low-resolution counterpart, we consider a simple toy example. The right panel of Figure 3 shows a synthetic two-class dataset. High-resolution points are sampled from a bivariate normal distribution and low-resolution points from the same distribution with one eighth of the variance. The motivation for this construction is shown in the left panel, where we take a subset of images from a single CIFAR-10 class, progressively downsample them to different spatial resolutions, flatten and standardise them, and project them onto a two-dimensional space using PCA. We then compute the variance of these low-dimensional representations as a function of resolution. Since the variance increases with resolution, lower-resolution observations occupy a more concentrated region of feature space, motivating the synthetic data generation procedure. We classify the two synthetic classes using linear discriminant analysis [Fisher, 1936], which enables closed-form computation of parameter changes. Each point is scaled according to the magnitude of the parameter change induced by including that datapoint in the training set. Low-resolution points, being more densely clustered, typically induce smaller parameter changes, whereas high-resolution points can be more influential when they lie outside the support of the low-resolution distribution. This illustrates the intuition behind our theoretical results: datapoint influence depends on the information lost under downsampling.

5 Experimental Setup

We empirically evaluate whether the theoretical differences between high- and low-resolution datapoints translate into measurable gains in practice. We study mixed-resolution training when high-resolution data is scarce, varying both the proportion of high-resolution samples and the resolution of the low-resolution data. This allows us to assess when low-resolution data is most useful and how its benefit depends on model architecture.

In all experiments, the dataset contains two resolutions. The low-resolution inputs are the low-frequency coefficients after low-pass filtering, corresponding to $\tilde{x}_l \in \mathbb{R}^t$ in Section 3. Accordingly, models are trained directly on \tilde{x}_l rather than on the embedded representation $x_l \in \mathbb{R}^s$ used in the theoretical analysis. We conduct four types of experiments on three datasets: CIFAR10/CIFAR100 [Krizhevsky, 2009] and AudioMNIST [Becker et al., 2024]. Since our focus is on regimes where high-resolution data is scarce, we use smaller benchmark datasets that allow controlled variation of the proportion of high- and low-resolution samples. In this setting, the relevant question is not whether low-resolution data is helpful when high-resolution data is abundant, but whether it can improve performance when high-resolution data is limited. The experiments are: **Subset**, train on all subsets from 10%-90% on full resolution, **Ratio**, perform mixed resolution training with a high-resolution ratio ranging from 10%-90%, **Downsampled**, train on the full dataset downsampled to a lower resolution, **Size**, perform mixed resolution training with a fixed high resolution ratio of 10% where the low-resolution size changes.

Full resolution for CIFAR is a square resolution of $L = 32$ and selected low resolutions are $L \in \{4, 8, 12, 16, 20\}$. To roughly correspond with the same level of downsampling while still complying

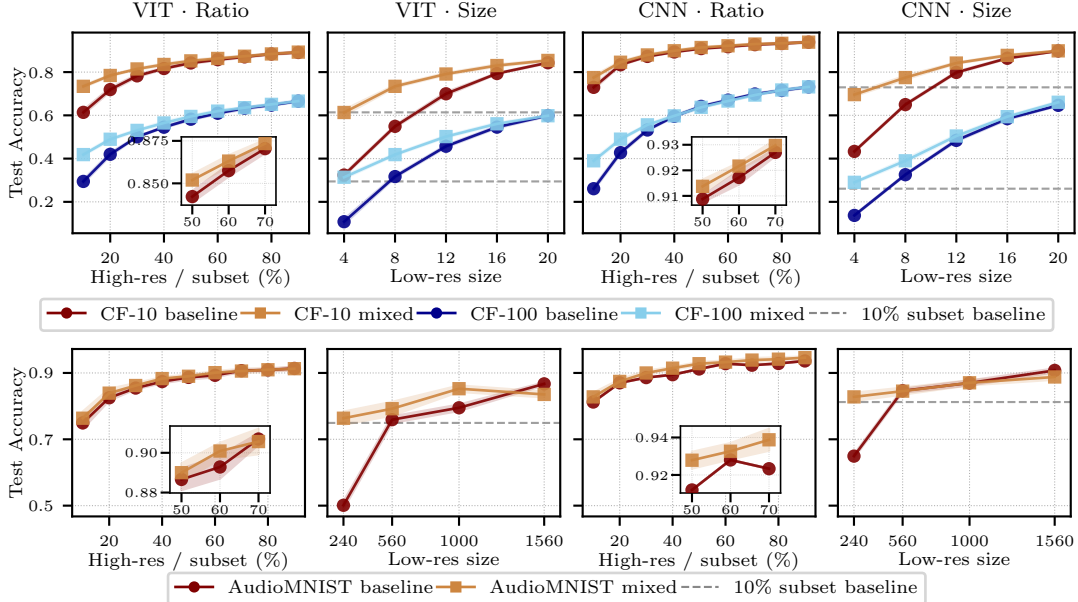


Figure 4: Effect of adding low-resolution data under varying levels of high-resolution scarcity. Ratio compares mixed-resolution training with high-resolution subsets only as the proportion of high-resolution samples increases. Size compares mixed-resolution training with fully downsampled training while varying the low-resolution input size at a fixed 10% high-resolution ratio; the 10% high-resolution subset baseline is shown in grey. CF denotes CIFAR. Mixed-resolution training consistently improves performance across datasets and architectures

with the networks, full resolution for AudioMNIST is 4000 Hz (downsampled from 8000 Hz) and chosen low resolutions are 1560 Hz, 1000 Hz, 560 Hz, and 240 Hz. To avoid overly high accuracy at low subsets, the AudioMNIST training set is reduced from 18,000 to 5,000. Ratio experiments are run with a low-resolution size of $8L$ for CIFAR and 240 Hz for AudioMNIST. All reported results are averaged over five independent runs with different random seeds, using the dataset-provided hold-out test sets. For more details regarding the training procedure, see Appendix F.

For the transformer-based experiments, we modify the ViT architecture from Yoshioka [2024]. For the CIFAR datasets we use a depth of 8, an attention head number of 6, and a patch size of 4. For AudioMNIST the ViT is modified to handle 1D inputs and has a depth of 4, an attention head number of 4, and a patch size of 8. Both networks are configured with a combination of fixed sinusoidal PEs and learnable ones. CNN-based experiments on CIFAR are conducted using the ResNet-18 architecture, where the initial max-pooling layer is removed and first kernel size is changed from 7 to 3 to better accommodate smaller input resolutions. For AudioMNIST the model proposed in the original paper is used with the addition of an adaptive pooling to adapt to different input resolutions (see code in the supplementary material).

6 Empirical Results

Figure 4 summarises the main empirical findings of this work (ablation studies are reported in Appendix F). The Ratio experiments are compared against Subset, while the Size experiments are compared against Downsampled. Across architectures and datasets, mixed-resolution training consistently improves performance, with gains diminishing as the proportion of high-resolution data increases. On the CIFAR datasets, the ViT benefits more from the addition of low-resolution data, whereas on AudioMNIST the CNN benefits more. One possible explanation is that CNNs rely more heavily on local spatial structure, which can be disrupted by coarse downsampling, thereby reducing the benefit of low-resolution data on the vision tasks. Overall, these results suggest that the benefit of mixed-resolution training depends not only on how much information is lost under downsampling, but also on how this loss interacts with the inductive biases of the model architecture.

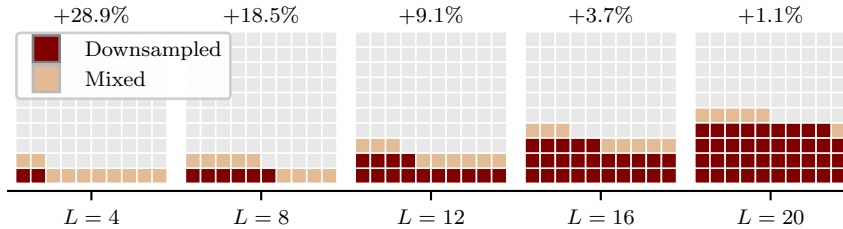


Figure 5: Trade-off between accuracy gain and storage cost for the Size experiment compared to the Downsampled on CIFAR-10 using the ViT. The 10×10 grid represents storage of the full dataset at full resolution, red cells correspond to storage of the downsampled regime, and yellow cells to additional storage for the mixed-resolution regime. For $L = 12$, the downsampled dataset uses $12^2/32^2 = 0.14$ of full storage, while the mixed dataset uses $(12^2 \cdot 0.9 + 32^2 \cdot 0.1)/32^2 = 0.226$. Storage ratios are rounded up to the nearest percentage point. The percentage above each panel denotes the relative improvement in classification accuracy achieved by the mixed approach.

While Figure 4 highlights the performance benefits of incorporating low-resolution data, it does not account for the associated storage costs. Figure 5 addresses this trade-off by visualising the additional storage required when storing 10% of the data at full resolution compared to a fully downsampled dataset, as in the Size experiments. The red squares indicate how much storage is used by the downsampled dataset relative to the full dataset (consisting purely of high-resolution data), which is illustrated by the 100 grey boxes. The yellow squares illustrate the additional storage required when 10% of the data is stored at full resolution. The results show that even small amounts of high-resolution data can yield substantial improvements in accuracy.

Taken together, figures 4 and 5 illustrate the performance-storage trade-offs of mixed-resolution training. The Ratio experiment shows that, when high-resolution data is scarce, collecting more low-resolution data can be more beneficial than acquiring a few additional high-resolution samples. Conversely, the Size experiment shows that selectively adding high-resolution samples can be more effective than uniformly increasing the resolution of the entire dataset.

7 Conclusion

In this work, we studied mixed-resolution training, where only a subset of the training data is available at high resolution, while the remaining data is observed in a downsampled form and evaluation is performed on high-resolution inputs. We showed theoretically that the contribution of a high-resolution datapoint relative to its low-resolution counterpart is governed both by the information missing from the low-resolution representation and by the sensitivity of the loss to that missing information. Empirically, across datasets, modalities, and model architectures, we found that incorporating low-resolution data consistently improves performance when high-resolution data is scarce. These results clearly demonstrate that low-resolution observations can retain useful task-relevant signal. The findings suggest that mixed-resolution training is a practical learning regime for settings constrained by storage, bandwidth, or data sharing, and motivate further study on larger and more naturally heterogeneous datasets.

8 Limitations

A limitation of the theoretical analysis is its reliance on local linear approximations of the loss with respect to the input, which are most accurate when the low-resolution input remains close to the high-resolution one. Nonetheless, the empirical results suggest that low-resolution data can still provide a useful learning signal even under more aggressive downsampling. A further limitation is that the empirical evaluation is restricted to relatively small-scale benchmarks. This was a deliberate design choice, as CIFAR-10/100 and AudioMNIST allow controlled study of mixed-resolution training in regimes where high-resolution data is scarce, although they do not capture the full complexity of larger and more diverse real-world datasets.

References

- Sören Becker, Johanna Vielhaben, Marcel Ackermann, Klaus-Robert Müller, Sebastian Lapuschkin, and Wojciech Samek. AudioMNIST: Exploring Explainable Artificial Intelligence for audio analysis on a simple benchmark. *Journal of the Franklin Institute*, 361(1):418–428, January 2024. ISSN 00160032. doi: 10.1016/j.jfranklin.2023.11.038. URL <https://linkinghub.elsevier.com/retrieve/pii/S0016003223007536>.
- Thomas Chang, Bahareh Tolooshams, and Demba Ba. Randnet: Deep Learning with Compressed Measurements of Images. In *2019 IEEE 29th International Workshop on Machine Learning for Signal Processing (MLSP)*, pages 1–6, Pittsburgh, PA, USA, October 2019. IEEE. ISBN 978-1-7281-0824-7. doi: 10.1109/MLSP.2019.8918878. URL <https://ieeexplore.ieee.org/document/8918878/>.
- Peng Chen, Yingying Zhang, Yunyao Cheng, Yang Shu, Yihang Wang, Qingsong Wen, Bin Yang, and Chenjuan Guo. Pathformer: Multi-scale Transformers with Adaptive Pathways for Time Series Forecasting, September 2024. URL <http://arxiv.org/abs/2402.05956>. arXiv:2402.05956 [cs].
- Jeppe Høy Christensen, Gabrielle H. Saunders, Lena Havtorn, and Niels H. Pontoppidan. Real-World Hearing Aid Usage Patterns and Smartphone Connectivity. *Frontiers in Digital Health*, 3:722186, August 2021. ISSN 2673-253X. doi: 10.3389/fdgth.2021.722186. URL <https://www.frontiersin.org/articles/10.3389/fdgth.2021.722186/full>.
- Yongjie Chu, Touqeer Ahmad, George Bebis, and Lindu Zhao. Low-resolution face recognition with single sample per person. *Signal Processing*, 141:144–157, December 2017. ISSN 01651684. doi: 10.1016/j.sigpro.2017.05.012. URL <https://linkinghub.elsevier.com/retrieve/pii/S0165168417301834>.
- Tian Dong, Bo Zhao, and Lingjuan Lyu. Privacy for free: How does dataset condensation help privacy? In *International Conference on Machine Learning*, pages 5378–5396. PMLR, 2022.
- Alexey Dosovitskiy, Lucas Beyer, Alexander Kolesnikov, Dirk Weissenborn, Xiaohua Zhai, Thomas Unterthiner, Mostafa Dehghani, Matthias Minderer, Georg Heigold, Sylvain Gelly, Jakob Uszkoreit, and Neil Houlsby. An Image is Worth 16x16 Words: Transformers for Image Recognition at Scale, June 2021. URL <http://arxiv.org/abs/2010.11929>. arXiv:2010.11929 [cs].
- Soumia Zohra El Mestari, Gabriele Lenzini, and Huseyin Demirci. Preserving data privacy in machine learning systems. *Computers & Security*, 137:103605, February 2024. ISSN 01674048. doi: 10.1016/j.cose.2023.103605. URL <https://linkinghub.elsevier.com/retrieve/pii/S0167404823005151>.
- Alexander Fabisch, Yohannes Kassahun, Hendrik Wöhrle, and Frank Kirchner. Learning in compressed space. *Neural Networks*, 42:83–93, June 2013. ISSN 08936080. doi: 10.1016/j.neunet.2013.01.020. URL <https://linkinghub.elsevier.com/retrieve/pii/S089360801300035X>.
- Qihang Fan, Quanzeng You, Xiaotian Han, Yongfei Liu, Yunzhe Tao, Huaibo Huang, Ran He, and Hongxia Yang. ViTAR: Vision Transformer with Any Resolution, March 2024. URL <http://arxiv.org/abs/2403.18361>. arXiv:2403.18361 [cs].
- Congyu Fang, Adam Dziedzic, Lin Zhang, Laura Oliva, Amol Verma, Fahad Razak, Nicolas Papernot, and Bo Wang. Decentralised, collaborative, and privacy-preserving machine learning for multi-hospital data. *eBioMedicine*, 101:105006, March 2024. ISSN 23523964. doi: 10.1016/j.ebiom.2024.105006. URL <https://linkinghub.elsevier.com/retrieve/pii/S2352396424000410>.
- R. A. Fisher. The use of multiple measurements in taxonomic problems. *Annals of Eugenics*, 7(2):179–188, 1936. doi: <https://doi.org/10.1111/j.1469-1809.1936.tb02137.x>. URL <https://onlinelibrary.wiley.com/doi/abs/10.1111/j.1469-1809.1936.tb02137.x>.

- Pedro Galeano, Esdras Joseph, and Rosa E. Lillo. The Mahalanobis Distance for Functional Data With Applications to Classification. *Technometrics*, 57(2):281–291, April 2015. ISSN 0040-1706, 1537-2723. doi: 10.1080/00401706.2014.902774. URL <http://www.tandfonline.com/doi/full/10.1080/00401706.2014.902774>.
- Shiming Ge, Shengwei Zhao, Chenyu Li, and Jia Li. Low-Resolution Face Recognition in the Wild via Selective Knowledge Distillation. *IEEE Transactions on Image Processing*, 28(4): 2051–2062, April 2019. ISSN 1057-7149, 1941-0042. doi: 10.1109/TIP.2018.2883743. URL <https://ieeexplore.ieee.org/document/8554301/>.
- Allan Gut. *Probability: A Graduate Course: A Graduate Course*, volume 75 of *Springer Texts in Statistics*. Springer New York, New York, NY, 2013. ISBN 978-1-4614-4707-8 978-1-4614-4708-5. doi: 10.1007/978-1-4614-4708-5. URL <https://link.springer.com/10.1007/978-1-4614-4708-5>.
- Zheng Hui, Xinbo Gao, Yunchu Yang, and Xiumei Wang. Lightweight Image Super-Resolution with Information Multi-distillation Network. In *Proceedings of the 27th ACM International Conference on Multimedia*, pages 2024–2032, Nice France, October 2019. ACM. ISBN 978-1-4503-6889-6. doi: 10.1145/3343031.3351084. URL <https://dl.acm.org/doi/10.1145/3343031.3351084>.
- Maurice George Kendall. *The advanced theory of statistics*. 1943.
- Michał Koziarski and Bogusław Cyganek. Impact of Low Resolution on Image Recognition with Deep Neural Networks: An Experimental Study. *International Journal of Applied Mathematics and Computer Science*, 28(4):735–744, December 2018. ISSN 2083-8492. doi: 10.2478/amcs-2018-0056. URL <https://www.sciendo.com/article/10.2478/amcs-2018-0056>.
- Alex Krizhevsky. Learning multiple layers of features from tiny images. 2009. URL <https://api.semanticscholar.org/CorpusID:18268744>.
- S. Kullback and R. A. Leibler. On Information and Sufficiency. *The Annals of Mathematical Statistics*, 22(1):79 – 86, 1951. doi: 10.1214/aoms/1177729694. URL <https://doi.org/10.1214/aoms/1177729694>.
- Y. LeCun, B. Boser, J. S. Denker, D. Henderson, R. E. Howard, W. Hubbard, and L. D. Jackel. Backpropagation Applied to Handwritten Zip Code Recognition. *Neural Computation*, 1(4): 541–551, December 1989. ISSN 0899-7667, 1530-888X. doi: 10.1162/neco.1989.1.4.541. URL <https://direct.mit.edu/neco/article/1/4/541-551/5515>.
- Ze Lu, Xudong Jiang, and Alex Kot. Deep Coupled ResNet for Low-Resolution Face Recognition. *IEEE Signal Processing Letters*, 25(4):526–530, April 2018. ISSN 1070-9908, 1558-2361. doi: 10.1109/LSP.2018.2810121. URL <http://ieeexplore.ieee.org/document/8303213/>.
- Stéphane Mallat. *A Wavelet Tour of Signal Processing*. Academic Press, 2009. ISBN 978-0-12-374370-1. doi: 10.1016/B978-0-12-374370-1.X0001-8.
- Sivaram Prasad Mudunuri and Soma Biswas. Low Resolution Face Recognition Across Variations in Pose and Illumination. *IEEE Transactions on Pattern Analysis and Machine Intelligence*, 38(5): 1034–1040, May 2016. ISSN 0162-8828, 2160-9292. doi: 10.1109/TPAMI.2015.2469282. URL <http://ieeexplore.ieee.org/document/7208853/>.
- Sarthak Pati, Sourav Kumar, Amokh Varma, Brandon Edwards, Charles Lu, Liangqiong Qu, Justin J. Wang, Anantharaman Lakshminarayanan, Shih-han Wang, Micah J. Sheller, Ken Chang, Praveer Singh, Daniel L. Rubin, Jayashree Kalpathy-Cramer, and Spyridon Bakas. Privacy preservation for federated learning in health care. *Patterns*, 5(7):100974, July 2024. ISSN 26663899. doi: 10.1016/j.patter.2024.100974. URL <https://linkinghub.elsevier.com/retrieve/pii/S2666389924000825>.
- Xingchao Peng, Judy Hoffman, Stella X. Yu, and Kate Saenko. Fine-to-coarse Knowledge Transfer For Low-Res Image Classification, May 2016. URL <http://arxiv.org/abs/1605.06695>. arXiv:1605.06695 [cs].

- Niels Henrik Pontoppidan, Xi Li, Lars Bramsløw, Benjamin Johansen, Claus Nielsen, Atefeh Hafez, and Michael Kai Petersen. Data-driven hearing care with time-stamped data-logging. *Proceedings of the International Symposium on Auditory and Audiological Research*, 6:127–134, February 2018. URL <https://proceedings.isaar.eu/index.php/isaarproc/article/view/2017-15>.
- Alexandre Sablayrolles, Matthijs Douze, Yann Ollivier, Cordelia Schmid, and Herve Jegou. White-box vs Black-box: Bayes Optimal Strategies for Membership Inference. *ICML*, 2019.
- Chitwan Saharia, Jonathan Ho, William Chan, Tim Salimans, David J. Fleet, and Mohammad Norouzi. Image Super-Resolution Via Iterative Refinement. *IEEE Transactions on Pattern Analysis and Machine Intelligence*, pages 1–14, 2022. ISSN 0162-8828, 2160-9292, 1939-3539. doi: 10.1109/TPAMI.2022.3204461. URL <https://ieeexplore.ieee.org/document/9887996/>.
- Rui Tian, Zuxuan Wu, Qi Dai, Han Hu, Yu Qiao, and Yu-Gang Jiang. ResFormer: Scaling ViTs with Multi-Resolution Training. In *2023 IEEE/CVF Conference on Computer Vision and Pattern Recognition (CVPR)*, pages 22721–22731, Vancouver, BC, Canada, June 2023. IEEE. ISBN 979-8-3503-0129-8. doi: 10.1109/CVPR52729.2023.02176. URL <https://ieeexplore.ieee.org/document/10204550/>.
- Yihe Wang, Nan Huang, Taida Li, Yujun Yan, and Xiang Zhang. Medformer: A multi-granularity patching transformer for medical time-series classification. *Advances in Neural Information Processing Systems*, 37:36314–36341, 2024.
- Zhangyang Wang, Shiyu Chang, Yingzhen Yang, Ding Liu, and Thomas S. Huang. Studying Very Low Resolution Recognition Using Deep Networks. In *2016 IEEE Conference on Computer Vision and Pattern Recognition (CVPR)*, pages 4792–4800, Las Vegas, NV, USA, June 2016. IEEE. ISBN 978-1-4673-8851-1. doi: 10.1109/CVPR.2016.518. URL <http://ieeexplore.ieee.org/document/7780887/>.
- Zhaowen Wang, Ding Liu, Jianchao Yang, Wei Han, and Thomas Huang. Deep Networks for Image Super-Resolution with Sparse Prior. In *2015 IEEE International Conference on Computer Vision (ICCV)*, pages 370–378, Santiago, Chile, December 2015. IEEE. ISBN 978-1-4673-8391-2. doi: 10.1109/ICCV.2015.50. URL <http://ieeexplore.ieee.org/document/7410407/>.
- Rizwan Uz Zaman Wani and Ozgu Can. FED-EHR: A Privacy-Preserving Federated Learning Framework for Decentralized Healthcare Analytics. *Electronics*, 14(16):3261, August 2025. ISSN 2079-9292. doi: 10.3390/electronics14163261. URL <https://www.mdpi.com/2079-9292/14/16/3261>.
- Fuwei Yang, Wenming Yang, Riqiang Gao, and Qingmin Liao. Discriminative Multidimensional Scaling for Low-Resolution Face Recognition. *IEEE Signal Processing Letters*, 25(3):388–392, March 2018. ISSN 1070-9908, 1558-2361. doi: 10.1109/LSP.2017.2746658. URL <https://ieeexplore.ieee.org/document/8022987/>.
- Kentaro Yoshioka. vision-transformers-cifar10: Training Vision Transformers (ViT) and related models on CIFAR-10, 2024. URL <https://github.com/kentaroy47/vision-transformers-cifar10>.
- Syed Waqas Zamir, Aditya Arora, Salman Khan, Munawar Hayat, Fahad Shahbaz Khan, Ming-Hsuan Yang, and Ling Shao. Learning Enriched Features for Real Image Restoration and Enhancement. In Andrea Vedaldi, Horst Bischof, Thomas Brox, and Jan-Michael Frahm, editors, *Computer Vision – ECCV 2020*, volume 12370, pages 492–511. Springer International Publishing, Cham, 2020. ISBN 978-3-030-58594-5 978-3-030-58595-2. doi: 10.1007/978-3-030-58595-2_30. URL https://link.springer.com/10.1007/978-3-030-58595-2_30. Series Title: Lecture Notes in Computer Science.
- Erfan Zangeneh, Mohammad Rahmati, and Yalda Mohsenzadeh. Low resolution face recognition using a two-branch deep convolutional neural network architecture. *Expert Systems with Applications*, 139:112854, January 2020. ISSN 09574174. doi: 10.1016/j.eswa.2019.112854. URL <https://linkinghub.elsevier.com/retrieve/pii/S0957417419305561>.

Fadila Zerka, Samir Barakat, Sean Walsh, Marta Bogowicz, Ralph T. H. Leijenaar, Arthur Jochems, Benjamin Miraglio, David Townend, and Philippe Lambin. Systematic Review of Privacy-Preserving Distributed Machine Learning From Federated Databases in Health Care. *JCO Clinical Cancer Informatics*, (4):184–200, November 2020. ISSN 2473-4276. doi: 10.1200/CCI.19.00047. URL <https://ascopubs.org/doi/10.1200/CCI.19.00047>.

Yitian Zhang, Liheng Ma, Soumyasundar Pal, Yingxue Zhang, and Mark Coates. Multi-resolution time-series transformer for long-term forecasting. In *International conference on artificial intelligence and statistics*, pages 4222–4230. PMLR, 2024.

Feng Zhao and Song Fan. Protecting Infinite Data Streams from Wearable Devices with Local Differential Privacy Techniques. *Information*, 15(10):630, October 2024. ISSN 2078-2489. doi: 10.3390/info15100630. URL <https://www.mdpi.com/2078-2489/15/10/630>.

A Theoretical Results

We start by state some additional definitions and technical terms.

A.1 Preliminary

Additional definitions

- (A1) The Kullback-Leibler divergence for two probability distributions p and q has the following definition [Kullback and Leibler, 1951]:

$$\text{KL}(p \parallel q) = \int p(\boldsymbol{\theta}) \log \left(\frac{p(\boldsymbol{\theta})}{q(\boldsymbol{\theta})} \right) d\boldsymbol{\theta}. \quad (9)$$

- (A2) A function, f , is locally linear if it can be written as:

$$f(\mathbf{x}) = f(\mathbf{a}) + \nabla^\top f(\mathbf{a})(\mathbf{x} - \mathbf{a}) + h_1(\mathbf{x}) \|\mathbf{x} - \mathbf{a}\|, \quad \lim_{\mathbf{x} \rightarrow \mathbf{a}} h_1(\mathbf{x}) = 0. \quad (10)$$

In the following derivations we consider the h_1 term to be negligible.

- (A3) The Cauchy–Schwarz inequality for variances for random variables X and Y is given by [Gut, 2013]:

$$|\text{Cov}[X, Y]| \leq \sqrt{\text{Var}[X]\text{Var}[Y]} \iff \quad (11)$$

$$-\sqrt{\text{Var}[X]\text{Var}[Y]} \leq \text{Cov}[X, Y] \leq \sqrt{\text{Var}[X]\text{Var}[Y]} \quad (12)$$

- (A4) The variance of a vector product for a vector \mathbf{a} and \mathbf{x} is $\text{Var}[\mathbf{a}^\top \mathbf{x}] = \mathbf{x}^\top \Sigma_{\mathbf{a}} \mathbf{x}$, where $\Sigma_{\mathbf{a}}$ is the covariance matrix of \mathbf{a} :

$$\begin{aligned} \text{Var}[\mathbf{a}^\top \mathbf{x}] &= \mathbb{E} \left[(\mathbf{a}^\top \mathbf{x} - \mathbb{E}[\mathbf{a}^\top \mathbf{x}])^2 \right] \\ &= \mathbb{E} \left[(\mathbf{a}^\top \mathbf{x} - \mathbb{E}[\mathbf{a}]^\top \mathbf{x})^2 \right] \\ &= \mathbb{E} \left[((\mathbf{a}^\top - \mathbb{E}[\mathbf{a}]^\top) \mathbf{x})^2 \right] \\ &= \mathbb{E} \left[\mathbf{x}^\top (\mathbf{a}^\top - \mathbb{E}[\mathbf{a}]^\top)^\top (\mathbf{a}^\top - \mathbb{E}[\mathbf{a}]^\top) \mathbf{x} \right] \\ &= \mathbb{E} \left[\mathbf{x}^\top (\mathbf{a} - \mathbb{E}[\mathbf{a}]) (\mathbf{a} - \mathbb{E}[\mathbf{a}])^\top \mathbf{x} \right] \\ &= \mathbf{x}^\top \mathbb{E} \left[(\mathbf{a} - \mathbb{E}[\mathbf{a}]) (\mathbf{a} - \mathbb{E}[\mathbf{a}])^\top \right] \mathbf{x} \\ &= \mathbf{x}^\top \Sigma_{\mathbf{a}} \mathbf{x} \end{aligned}$$

- (A5) Let $\|\mathbf{x}\|_A$ denote the Mahalanobis distance from the zero vector to a point \mathbf{x} given by $\mathbf{x}^\top A \mathbf{x} = \|\mathbf{x}\|_A^2$ for a non-singular matrix A [Galeano et al., 2015].

A datapoint consists of an observation \mathbf{x} and a target y . The loss function is written in short as $\ell(\boldsymbol{\theta}, \mathbf{x}) = \ell(\boldsymbol{\theta}; \mathbf{x}, y)$ such that the target is implicit. For all derivatives it is implied they are taken with respect to the observation, \mathbf{x} and not the target.

Throughout the theoretical analysis, the datapoints \mathbf{x}_h and \mathbf{x}_l are treated as fixed, and the only source of randomness are the model parameters $\boldsymbol{\theta}$.

A.2 Proof of Proposition 3

Let $\mathcal{X} = \{\mathbf{x}_1, \mathbf{x}_2, \dots, \mathbf{x}_N\}$ be a dataset consisting of samples of different resolutions. We introduce $\mathcal{X}_h = \mathcal{X} \cup \{\mathbf{x}_h\}$ and $\mathcal{X}_l = \mathcal{X} \cup \{\mathbf{x}_l\}$, where \mathbf{x}_h and \mathbf{x}_l denote the same underlying datapoint observed at high and low resolution, respectively.

Under Assumption 1, the model parameters conditioned on the dataset \mathcal{X} follow the distribution:

$$p(\boldsymbol{\theta} \mid \mathcal{X}) = \frac{1}{Z(\mathcal{X})} \exp \left(-\frac{1}{\gamma} \sum_{i=1}^N \ell(\boldsymbol{\theta}, \mathbf{x}_i) \right), \quad (13)$$

where, without loss of generality, we set $\gamma = 1$. For notational convenience, define $Z := Z(\mathcal{X})$, $Z_h := Z(\mathcal{X} \cup \{\mathbf{x}_h\})$ and $Z_l := Z(\mathcal{X} \cup \{\mathbf{x}_l\})$. Then the distribution of the model parameters when adding \mathbf{x}_h is,

$$p(\boldsymbol{\theta} \mid \mathcal{X}_h) = \frac{1}{Z_h} \exp \left(- \sum_{i=1}^N \ell(\boldsymbol{\theta}, \mathbf{x}_i) - \ell(\boldsymbol{\theta}, \mathbf{x}_h) \right), \quad (14)$$

The distribution can likewise be found for adding \mathbf{x}_l . It follows that the ratio between the two distributions can be written as

$$\frac{p(\boldsymbol{\theta} \mid \mathcal{X})}{p(\boldsymbol{\theta} \mid \mathcal{X}_h)} = \frac{Z_h}{Z} \exp(\ell(\boldsymbol{\theta}, \mathbf{x}_h)). \quad (15)$$

The KL-divergence corresponding to the inclusion of \mathbf{x}_h

$$\text{KL}_h = \mathbb{E}_{\boldsymbol{\theta} \mid \mathcal{X}} \left[\log \left(\frac{p(\boldsymbol{\theta} \mid \mathcal{X})}{p(\boldsymbol{\theta} \mid \mathcal{X}_h)} \right) \right], \quad (16)$$

which simplifies to

$$\text{KL}_h = \log \left(\frac{Z_h}{Z} \right) + \mathbb{E}_{\boldsymbol{\theta} \mid \mathcal{X}}[\ell(\boldsymbol{\theta}, \mathbf{x}_h)]. \quad (17)$$

An identical argument yields

$$\text{KL}_l = \log \left(\frac{Z_l}{Z} \right) + \mathbb{E}_{\boldsymbol{\theta} \mid \mathcal{X}}[\ell(\boldsymbol{\theta}, \mathbf{x}_l)]. \quad (18)$$

To identify the ratio Z_h/Z , similarly Z_l/Z , we note that the ratio between the two distributions can be written as (15). Rearranging and integrating over both sides yields

$$\int p(\boldsymbol{\theta} \mid \mathcal{X}_h) d\boldsymbol{\theta} = \frac{Z}{Z_h} \int p(\boldsymbol{\theta} \mid \mathcal{X}) \exp(-\ell(\boldsymbol{\theta}, \mathbf{x}_h)) d\boldsymbol{\theta}, \quad (19)$$

hence

$$\frac{Z_h}{Z} = \mathbb{E}_{\boldsymbol{\theta} \mid \mathcal{X}}[\exp(-\ell(\boldsymbol{\theta}, \mathbf{x}_h))]. \quad (20)$$

Substituting these expressions into the formulas for KL_h and KL_l yields the desired result:

$$\frac{\text{KL}_h}{\text{KL}_l} = \frac{\log(\mathbb{E}_{\boldsymbol{\theta} \mid \mathcal{X}}[\exp(-\ell(\boldsymbol{\theta}, \mathbf{x}_h))]) + \mathbb{E}_{\boldsymbol{\theta} \mid \mathcal{X}}[\ell(\boldsymbol{\theta}, \mathbf{x}_h)]}{\log(\mathbb{E}_{\boldsymbol{\theta} \mid \mathcal{X}}[\exp(-\ell(\boldsymbol{\theta}, \mathbf{x}_l))]) + \mathbb{E}_{\boldsymbol{\theta} \mid \mathcal{X}}[\ell(\boldsymbol{\theta}, \mathbf{x}_l)]}. \quad (21)$$

A.3 Proof of Proposition 4

The cumulant generating function of a random variable Y is given by [Kendall, 1943]

$$K_Y(b) := \log \mathbb{E}[e^{bY}] = \sum_{n=1}^{\infty} \kappa_n \frac{b^n}{n!}, \quad (22)$$

where κ_n denotes the n th cumulant of Y . Truncating this expansion at second order yields the approximation

$$K_Y(b) \approx \kappa_1 b + \kappa_2 \frac{b^2}{2} = \mathbb{E}[Y]b + \frac{b^2}{2} \text{Var}[Y]. \quad (23)$$

For a fixed datapoint \mathbf{x} , define the random variable

$$Y_{\mathbf{x}} := \ell(\boldsymbol{\theta}, \mathbf{x}), \quad \boldsymbol{\theta} \sim p(\boldsymbol{\theta} \mid \mathcal{X}). \quad (24)$$

Since the expectation of a function, h , is $\mathbb{E}[h(x)] = \int h(x)p(x) dx$ then

$$\mathbb{E}_{\boldsymbol{\theta} \mid \mathcal{X}}[h(\boldsymbol{\theta})] = \int_{\Theta} h(\boldsymbol{\theta}) p(\boldsymbol{\theta} \mid \mathcal{X}) d\boldsymbol{\theta}, \quad (25)$$

for any integrable function h . Setting $b = -1$ and $Y = Y_{\mathbf{x}}$ in eq. (23) yields

$$K_{Y_{\mathbf{x}}}(-1) \approx -\mathbb{E}_{\boldsymbol{\theta}|\mathcal{X}}[\ell(\boldsymbol{\theta}, \mathbf{x})] + \frac{1}{2}\text{Var}_{\boldsymbol{\theta}|\mathcal{X}}[\ell(\boldsymbol{\theta}, \mathbf{x})], \quad (26)$$

since the first two cumulants satisfy $\kappa_1 = \mathbb{E}[Y]$ and $\kappa_2 = \text{Var}[Y]$. Applying this to $Y_{\mathbf{x}_l} = \ell(\boldsymbol{\theta}, \mathbf{x}_l)$ and $Y_{\mathbf{x}_h} = \ell(\boldsymbol{\theta}, \mathbf{x}_h)$ results in

$$\log \mathbb{E}_{\boldsymbol{\theta}|\mathcal{X}} \left[e^{-\ell(\boldsymbol{\theta}, \mathbf{x}_l)} \right] \approx -\mathbb{E}_{\boldsymbol{\theta}|\mathcal{X}} [\ell(\boldsymbol{\theta}, \mathbf{x}_l)] + \frac{1}{2}\text{Var}_{\boldsymbol{\theta}|\mathcal{X}} [\ell(\boldsymbol{\theta}, \mathbf{x}_l)], \quad (27)$$

$$\log \mathbb{E}_{\boldsymbol{\theta}|\mathcal{X}} \left[e^{-\ell(\boldsymbol{\theta}, \mathbf{x}_h)} \right] \approx -\mathbb{E}_{\boldsymbol{\theta}|\mathcal{X}} [\ell(\boldsymbol{\theta}, \mathbf{x}_h)] + \frac{1}{2}\text{Var}_{\boldsymbol{\theta}|\mathcal{X}} [\ell(\boldsymbol{\theta}, \mathbf{x}_h)]. \quad (28)$$

Substituting these approximations into (21) yields

$$\frac{\text{KL}_h}{\text{KL}_l} \approx \frac{\text{Var}_{\boldsymbol{\theta}|\mathcal{X}} [\ell(\boldsymbol{\theta}, \mathbf{x}_h)]}{\text{Var}_{\boldsymbol{\theta}|\mathcal{X}} [\ell(\boldsymbol{\theta}, \mathbf{x}_l)]}, \quad (29)$$

which is what we wanted to show.

A.4 Proof of Proposition 5

Starting from the result from Proposition 4:

$$\frac{\text{KL}_h}{\text{KL}_l} \approx \frac{\text{Var}_{\boldsymbol{\theta}|\mathcal{X}} [\ell(\boldsymbol{\theta}, \mathbf{x}_h)]}{\text{Var}_{\boldsymbol{\theta}|\mathcal{X}} [\ell(\boldsymbol{\theta}, \mathbf{x}_l)]}, \quad (30)$$

we use (A2) on the loss function:

$$\ell(\boldsymbol{\theta}, \mathbf{x}_h) = \ell(\boldsymbol{\theta}, \mathbf{x}_l + \mathbf{x}_r) \approx \ell(\boldsymbol{\theta}, \mathbf{x}_l) + \nabla_{\mathbf{x}}^{\top} \ell(\boldsymbol{\theta}, \mathbf{x}) \Big|_{\mathbf{x}=\mathbf{x}_l} \mathbf{x}_r, \quad (31)$$

where we introduce $\mathbf{g} = \nabla_{\mathbf{x}} \ell(\boldsymbol{\theta}, \mathbf{x}) \Big|_{\mathbf{x}=\mathbf{x}_l}$. A rewrite of the numerator of eq. (30) yields,

$$\text{Var}[\ell(\boldsymbol{\theta}, \mathbf{x}_h)] = \text{Var}[\ell(\boldsymbol{\theta}, \mathbf{x}_l)] + \text{Var}[\mathbf{g}^{\top} \mathbf{x}_r] + 2\text{Cov}[\ell(\boldsymbol{\theta}, \mathbf{x}_l), \mathbf{g}^{\top} \mathbf{x}_r]. \quad (32)$$

Lower bound the covariance using (A3):

$$\text{Var}[\ell(\boldsymbol{\theta}, \mathbf{x}_h)] \geq \text{Var}[\ell(\boldsymbol{\theta}, \mathbf{x}_l)] + \text{Var}[\mathbf{g}^{\top} \mathbf{x}_r] - 2\sqrt{\text{Var}[\ell(\boldsymbol{\theta}, \mathbf{x}_l)]\text{Var}[\mathbf{g}^{\top} \mathbf{x}_r]}. \quad (33)$$

Introduce $\sigma_l^2 := \text{Var}[\ell(\boldsymbol{\theta}, \mathbf{x}_l)]$ and using (A4):

$$\frac{\text{KL}_h}{\text{KL}_l} \geq \frac{\sigma_l^2 + \mathbf{x}_r^{\top} \Sigma_{\mathbf{g}} \mathbf{x}_r - 2\sqrt{\sigma_l^2 \mathbf{x}_r^{\top} \Sigma_{\mathbf{g}} \mathbf{x}_r}}{\sigma_l^2}, \quad (34)$$

where using (A5) gives us the following lower bound:

$$\frac{\text{KL}_h}{\text{KL}_l} \geq \left(1 - \sqrt{\frac{\|\mathbf{x}_r\|_{\Sigma_{\mathbf{g}}}^2}{\sigma_l^2}} \right)^2. \quad (35)$$

Using (A3) to upper bound eq. (32) yields the corresponding upper bound:

$$\frac{\text{KL}_h}{\text{KL}_l} \leq \left(1 + \sqrt{\frac{\|\mathbf{x}_r\|_{\Sigma_{\mathbf{g}}}^2}{\sigma_l^2}} \right)^2. \quad (36)$$

A.5 Proof of Proposition 6

Starting from Definition (A1), we can write the difference between KL_h and KL_l as

$$\text{KL}_h - \text{KL}_l = \int p(\boldsymbol{\theta} | \mathcal{X}) \log \left(\frac{p(\boldsymbol{\theta} | \mathcal{X})}{p(\boldsymbol{\theta} | \mathcal{X}_h)} \right) d\boldsymbol{\theta} - \int p(\boldsymbol{\theta} | \mathcal{X}) \log \left(\frac{p(\boldsymbol{\theta} | \mathcal{X})}{p(\boldsymbol{\theta} | \mathcal{X}_l)} \right) d\boldsymbol{\theta} \quad (37)$$

$$= - \int p(\boldsymbol{\theta} | \mathcal{X}) \log (p(\boldsymbol{\theta} | \mathcal{X}_h)) d\boldsymbol{\theta} + \int p(\boldsymbol{\theta} | \mathcal{X}) \log (p(\boldsymbol{\theta} | \mathcal{X}_l)) d\boldsymbol{\theta} \quad (38)$$

$$= \int p(\boldsymbol{\theta} | \mathcal{X}) \log \left(\frac{p(\boldsymbol{\theta} | \mathcal{X}_l)}{p(\boldsymbol{\theta} | \mathcal{X}_h)} \right) d\boldsymbol{\theta}. \quad (39)$$

Under Assumption 1, the log term is expressed as:

$$\log \left(\frac{P(\boldsymbol{\theta} | \mathcal{X}_l)}{P(\boldsymbol{\theta} | \mathcal{X}_h)} \right) = \log \left(\frac{\frac{1}{Z_l} \exp \left(-\sum_{i=1}^N \ell(\boldsymbol{\theta}, \mathbf{x}_i) - \ell(\boldsymbol{\theta}, \mathbf{x}_l) \right)}{\frac{1}{Z_h} \exp \left(-\sum_{i=1}^N \ell(\boldsymbol{\theta}, \mathbf{x}_i) - \ell(\boldsymbol{\theta}, \mathbf{x}_h) \right)} \right) \quad (40)$$

$$= \log \left(\frac{Z_h}{Z_l} \right) + (\ell(\boldsymbol{\theta}, \mathbf{x}_h) - \ell(\boldsymbol{\theta}, \mathbf{x}_l)). \quad (41)$$

Introducing $\Delta(\boldsymbol{\theta}) = \ell(\boldsymbol{\theta}, \mathbf{x}_h) - \ell(\boldsymbol{\theta}, \mathbf{x}_l)$ for notational convenience. A rewrite of Z_h yields,

$$Z_h = \int \exp \left(-\sum_{i=1}^N \ell(\boldsymbol{\theta}, \mathbf{x}_i) - \ell(\boldsymbol{\theta}, \mathbf{x}_l) \right) \exp(\ell(\boldsymbol{\theta}, \mathbf{x}_l) - \ell(\boldsymbol{\theta}, \mathbf{x}_h)) d\boldsymbol{\theta} \quad (42)$$

$$= \int Z_l p(\boldsymbol{\theta} | \mathcal{X}_l) \exp(-\Delta(\boldsymbol{\theta})) d\boldsymbol{\theta} \quad (43)$$

$$= Z_l \mathbb{E}_{\boldsymbol{\theta} | \mathcal{X}_l} [\exp(-\Delta(\boldsymbol{\theta}))]. \quad (44)$$

Substitute back into eq. (41):

$$\log \left(\frac{Z_h}{Z_l} \right) + \Delta(\boldsymbol{\theta}) = \log (\mathbb{E}_{\boldsymbol{\theta} | \mathcal{X}_l} [\exp(-\Delta(\boldsymbol{\theta}))]) + \Delta(\boldsymbol{\theta}), \quad (45)$$

and subsequently into eq. (39), the difference in KL divergence admits the following closed-form expression:

$$\text{KL}_h - \text{KL}_l = \int p(\boldsymbol{\theta} | \mathcal{X}) (\log (\mathbb{E}_{\boldsymbol{\theta} | \mathcal{X}_l} [\exp(-\Delta(\boldsymbol{\theta}))]) + \Delta(\boldsymbol{\theta})) d\boldsymbol{\theta} \quad (46)$$

$$= \log (\mathbb{E}_{\boldsymbol{\theta} | \mathcal{X}_l} [\exp(-\Delta(\boldsymbol{\theta}))]) + \mathbb{E}_{\boldsymbol{\theta} | \mathcal{X}} [\Delta(\boldsymbol{\theta})]. \quad (47)$$

The use of the cumulant generating function used in Proposition 4 can similarly be applied here:

$$\text{KL}_h - \text{KL}_l \approx \frac{1}{2} \text{Var}_{\boldsymbol{\theta} | \mathcal{X}_l} [\Delta(\boldsymbol{\theta})] - \mathbb{E}_{\boldsymbol{\theta} | \mathcal{X}_l} [\Delta(\boldsymbol{\theta})] + \mathbb{E}_{\boldsymbol{\theta} | \mathcal{X}} [\Delta(\boldsymbol{\theta})] \quad (48)$$

To rewrite the last term to follow the same distribution as the first two, we find the relation between the two distributions:

$$\begin{aligned} \frac{p(\boldsymbol{\theta} | \mathcal{X})}{p(\boldsymbol{\theta} | \mathcal{X}_l)} &= \frac{Z_l}{Z} \exp(\ell(\boldsymbol{\theta}, \mathbf{x}_l)) \iff \\ p(\boldsymbol{\theta} | \mathcal{X}) &= \frac{Z_l}{Z} \exp(\ell(\boldsymbol{\theta}, \mathbf{x}_l)) p(\boldsymbol{\theta} | \mathcal{X}_l). \end{aligned}$$

Integration over $\boldsymbol{\theta}$ on both sides yields $Z_l/Z = (\mathbb{E}_{\boldsymbol{\theta} | \mathcal{X}_l} [\exp(\ell(\boldsymbol{\theta}, \mathbf{x}_l))])^{-1}$, such that if we multiply both sides with $\Delta(\boldsymbol{\theta})$ and integrate we get

$$\mathbb{E}_{\boldsymbol{\theta} | \mathcal{X}} [\Delta(\boldsymbol{\theta})] = \frac{\mathbb{E}_{\boldsymbol{\theta} | \mathcal{X}_l} [\exp(\ell(\boldsymbol{\theta}, \mathbf{x}_l)) \Delta(\boldsymbol{\theta})]}{\mathbb{E}_{\boldsymbol{\theta} | \mathcal{X}_l} [\exp(\ell(\boldsymbol{\theta}, \mathbf{x}_l))]} \quad (49)$$

Substitute back into (48):

$$\text{KL}_h - \text{KL}_l \approx \frac{1}{2} \text{Var}_{\boldsymbol{\theta} | \mathcal{X}_l} [\Delta(\boldsymbol{\theta})] - \mathbb{E}_{\boldsymbol{\theta} | \mathcal{X}_l} [\Delta(\boldsymbol{\theta})] + \frac{\mathbb{E}_{\boldsymbol{\theta} | \mathcal{X}_l} [\exp(\ell(\boldsymbol{\theta}, \mathbf{x}_l)) \Delta(\boldsymbol{\theta})]}{\mathbb{E}_{\boldsymbol{\theta} | \mathcal{X}_l} [\exp(\ell(\boldsymbol{\theta}, \mathbf{x}_l))]} \quad (50)$$

$$= \frac{1}{2} \text{Var}_{\boldsymbol{\theta} | \mathcal{X}_l} [\Delta(\boldsymbol{\theta})] + \frac{\mathbb{E}_{\boldsymbol{\theta} | \mathcal{X}_l} [\exp(\ell(\boldsymbol{\theta}, \mathbf{x}_l)) \Delta(\boldsymbol{\theta})] - \mathbb{E}_{\boldsymbol{\theta} | \mathcal{X}_l} [\Delta(\boldsymbol{\theta})] \mathbb{E}_{\boldsymbol{\theta} | \mathcal{X}_l} [\exp(\ell(\boldsymbol{\theta}, \mathbf{x}_l))]}{\mathbb{E}_{\boldsymbol{\theta} | \mathcal{X}_l} [\exp(\ell(\boldsymbol{\theta}, \mathbf{x}_l))]} \quad (51)$$

$$= \frac{1}{2} \text{Var}_{\boldsymbol{\theta} | \mathcal{X}_l} [\Delta(\boldsymbol{\theta})] + \frac{\text{Cov} [\Delta(\boldsymbol{\theta}), \exp(\ell(\boldsymbol{\theta}, \mathbf{x}_l))]}{\mathbb{E}_{\boldsymbol{\theta} | \mathcal{X}_l} [\exp(\ell(\boldsymbol{\theta}, \mathbf{x}_l))]} \quad (52)$$

Using (A2) on the loss function:

$$\ell(\boldsymbol{\theta}, \mathbf{x}_h) \approx \ell(\boldsymbol{\theta}, \mathbf{x}_l) + \nabla_{\mathbf{x}}^\top \ell(\boldsymbol{\theta}, \mathbf{x}) \Big|_{\mathbf{x}=\mathbf{x}_l} \mathbf{x}_r = \ell(\boldsymbol{\theta}, \mathbf{x}_l) + \mathbf{g}^\top \mathbf{x}_r, \quad (53)$$

introducing $\mathbf{g} = \nabla_{\mathbf{x}} \ell(\boldsymbol{\theta}, \mathbf{x})|_{\mathbf{x}=\mathbf{x}_l}$ such that $\Delta(\boldsymbol{\theta}) = \mathbf{g}^\top \mathbf{x}_r$. From this point onward in the derivation all expectations, variances and covariances are taken with respect to $P(\boldsymbol{\theta} | \mathcal{X} \cup \{\mathbf{x}_l\})$, and we will thus drop subscripts. We then obtain the following lower bound:

$$\begin{aligned} \text{KL}_h - \text{KL}_l &\approx \frac{1}{2} \text{Var}[\mathbf{g}^\top \mathbf{x}_r] + \frac{\text{Cov}[\mathbf{g}^\top \mathbf{x}_r, \exp(\ell(\boldsymbol{\theta}, \mathbf{x}_l))]}{\mathbb{E}[\exp(\ell(\boldsymbol{\theta}, \mathbf{x}_l))]} \\ &\stackrel{\text{(A3)}}{\geq} \frac{1}{2} \text{Var}[\mathbf{g}^\top \mathbf{x}_r] - \frac{\sqrt{\text{Var}[\exp(\ell(\boldsymbol{\theta}, \mathbf{x}_l))]}]{\mathbb{E}[\exp(\ell(\boldsymbol{\theta}, \mathbf{x}_l))]} \cdot \sqrt{\text{Var}[\mathbf{g}^\top \mathbf{x}_r]} \\ &\stackrel{\text{(A4)}+\text{(A5)}}{=} \frac{1}{2} \|\mathbf{x}_r\|_{\Sigma_g}^2 - \zeta \|\mathbf{x}_r\|_{\Sigma_g}, \end{aligned}$$

where $\zeta = \sqrt{\text{Var}_{\boldsymbol{\theta}|\mathcal{X} \cup \{\mathbf{x}_l\}}[\exp(\ell(\boldsymbol{\theta}, \mathbf{x}_l))]} / \mathbb{E}_{\boldsymbol{\theta}|\mathcal{X} \cup \{\mathbf{x}_l\}}[\exp(\ell(\boldsymbol{\theta}, \mathbf{x}_l))]$. The upper bound is found by upper bounding the covariance term using (A3) which results in

$$\text{KL}_h - \text{KL}_l \leq \frac{1}{2} \|\mathbf{x}_r\|_{\Sigma_g}^2 + \zeta \|\mathbf{x}_r\|_{\Sigma_g}. \quad (54)$$

B Additional Derivations

For notational simplicity, we add some additional definitions:

1. For a matrix $H \in \mathbb{R}^{s \times s}$ define $\Sigma_H := \text{Cov}[\text{vec}(H)]$
2. $Q_H(\mathbf{x}_r) := \left(\text{vec}(\mathbf{x}_r \mathbf{x}_r^\top)^\top \Sigma_H \text{vec}(\mathbf{x}_r \mathbf{x}_r^\top) \right)^{1/2}$

such that

$$\text{Var}[\mathbf{x}_r^\top H \mathbf{x}_r] = Q_H(\mathbf{x}_r)^2 \quad (55)$$

B.1 Second Order Approximations of Proofs

Here we provide proofs of Proposition 5-6 using a second order Taylor expansion.

Proposition 5 A second order Taylor expansion of the loss function yields:

$$\ell(\boldsymbol{\theta}, \mathbf{x}_h) = \ell(\boldsymbol{\theta}, \mathbf{x}_l + \mathbf{x}_r) \approx \ell(\boldsymbol{\theta}, \mathbf{x}_l) + \nabla_{\mathbf{x}} \ell(\boldsymbol{\theta}, \mathbf{x})|_{\mathbf{x}=\mathbf{x}_l}^\top \mathbf{x}_r + \frac{1}{2} \mathbf{x}_r^\top \nabla_{\mathbf{x}}^2 \ell(\boldsymbol{\theta}, \mathbf{x})|_{\mathbf{x}=\mathbf{x}_l} \mathbf{x}_r \quad (56)$$

$$= \ell(\boldsymbol{\theta}, \mathbf{x}_l) + \mathbf{g}^\top \mathbf{x}_r + \frac{1}{2} \mathbf{x}_r^\top H \mathbf{x}_r, \quad (57)$$

where $\mathbf{g} = \nabla_{\mathbf{x}} \ell(\boldsymbol{\theta}, \mathbf{x})|_{\mathbf{x}=\mathbf{x}_l}$ and $H := \nabla_{\mathbf{x}}^2 \ell(\boldsymbol{\theta}, \mathbf{x})|_{\mathbf{x}=\mathbf{x}_l}$. The numerator of eq. (30) is thus given by,

$$\begin{aligned} \text{Var}[\ell(\boldsymbol{\theta}, \mathbf{x}_h)] &= \text{Var}[\ell(\boldsymbol{\theta}, \mathbf{x}_l)] + \text{Var}[\mathbf{g}^\top \mathbf{x}_r] + \text{Var}\left[\frac{1}{2} \mathbf{x}_r^\top H \mathbf{x}_r\right] \\ &\quad + 2\text{Cov}[\ell(\boldsymbol{\theta}, \mathbf{x}_l), \mathbf{g}^\top \mathbf{x}_r] + 2\text{Cov}\left[\ell(\boldsymbol{\theta}, \mathbf{x}_l), \frac{1}{2} \mathbf{x}_r^\top H \mathbf{x}_r\right] + 2\text{Cov}\left[\mathbf{g}^\top \mathbf{x}_r, \frac{1}{2} \mathbf{x}_r^\top H \mathbf{x}_r\right]. \end{aligned}$$

Introducing $\sigma_l^2 := \text{Var}[\ell(\boldsymbol{\theta}, \mathbf{x}_l)]$. Apply (A4) and using (A3) to lower bound all covariances:

$$\begin{aligned} \text{Var}[\ell(\boldsymbol{\theta}, \mathbf{x}_h)] &\geq \sigma_l^2 + \mathbf{x}_r^\top \Sigma_g \mathbf{x}_r + \frac{1}{4} \text{vec}(\mathbf{x}_r \mathbf{x}_r^\top)^\top \Sigma_H \text{vec}(\mathbf{x}_r \mathbf{x}_r^\top) - 2\sqrt{\sigma_l^2 \mathbf{x}_r^\top \Sigma_g \mathbf{x}_r} \\ &\quad - \sqrt{\sigma_l^2 \text{vec}(\mathbf{x}_r \mathbf{x}_r^\top)^\top \Sigma_H \text{vec}(\mathbf{x}_r \mathbf{x}_r^\top)} - \sqrt{\mathbf{x}_r^\top \Sigma_g \mathbf{x}_r \text{vec}(\mathbf{x}_r \mathbf{x}_r^\top)^\top \Sigma_H \text{vec}(\mathbf{x}_r \mathbf{x}_r^\top)} \\ &\stackrel{\text{(A5)}}{=} \sigma_l^2 + \|\mathbf{x}_r\|_{\Sigma_g}^2 + \frac{1}{4} Q_H(\mathbf{x}_r)^2 \\ &\quad - 2\sigma_l \|\mathbf{x}_r\|_{\Sigma_g} - \sigma_l Q_H(\mathbf{x}_r) - \|\mathbf{x}_r\|_{\Sigma_g} Q_H(\mathbf{x}_r). \end{aligned}$$

Rearranging gives us the final lower bound:

$$\frac{\text{KL}_h}{\text{KL}_l} \geq \frac{(\sigma_l - \|\mathbf{x}_r\|_{\Sigma_g})^2 + \frac{1}{4} Q_H(\mathbf{x}_r)^2 - (\sigma_l Q_H(\mathbf{x}_r) + \|\mathbf{x}_r\|_{\Sigma_g} Q_H(\mathbf{x}_r))}{\sigma_l^2}. \quad (58)$$

Using (A3) to upper bound all covariances results in:

$$\frac{\text{KL}_h}{\text{KL}_l} \leq \frac{(\sigma_l + \|\mathbf{x}_r\|_{\Sigma_g})^2 + \frac{1}{4} Q_H(\mathbf{x}_r)^2 + (\sigma_l Q_H(\mathbf{x}_r) + \|\mathbf{x}_r\|_{\Sigma_g} Q_H(\mathbf{x}_r))}{\sigma_l^2}. \quad (59)$$

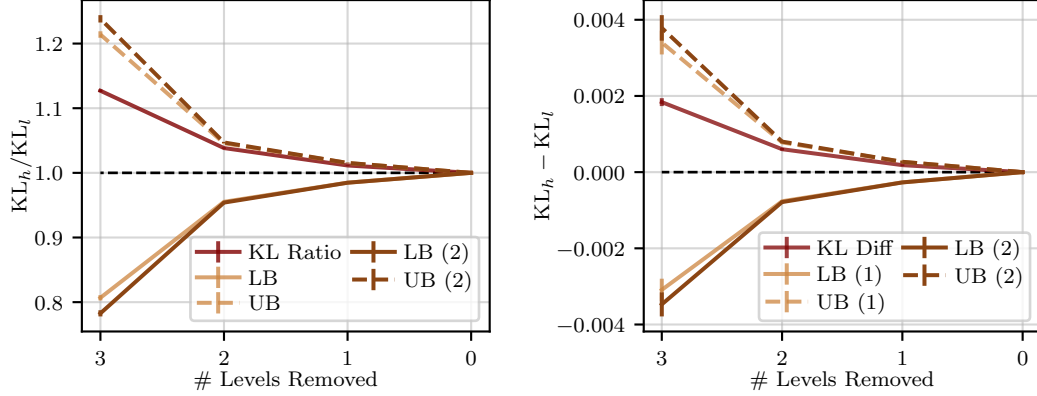


Figure 6: Simulation of bounds as a function of progressively removed high-frequency content. Error bars again denote five standard deviations. LB = Lower Bound, UB = Upper Bound with the order of approximation in parenthesis. There is no added benefit of going from a first to a second order Taylor expansion.

C Synthetic Data via Wavelets

To empirically validate the bounds derived in Proposition 5 and 6, we require data points that satisfy the decomposition:

$$\mathbf{x}_h = \mathbf{x}_l + \mathbf{x}_r, \quad (64)$$

where \mathbf{x}_h , \mathbf{x}_l and \mathbf{x}_r are in \mathbb{R}^s . We construct such data using the Discrete Wavelet Transform (DWT). The DWT provides an exact, non-redundant representation of a signal using a finite set of coefficients and enables lossless reconstruction via its inverse transform [Mallat, 2009]. It also yields a multi-resolution decomposition with basis functions localized in both time and frequency.

Given a signal $\mathbf{x} \in \mathbb{R}^s$, the DWT produces a set of coefficients $\{a_J, d_J, d_{J-1}, \dots, d_1\}$, where a_J denotes the approximation coefficients capturing low-frequency content, and d_j denotes the detail coefficients capturing progressively higher frequency components. We construct a low-resolution signal \mathbf{x}_l by applying the inverse DWT using only a subset of coefficients (e.g., a_J and selected d_j). The residual component \mathbf{x}_r is obtained by applying the inverse DWT to the complementary set of detail coefficients. Since the inverse DWT is linear and the coefficient sets form a disjoint partition, their reconstructions add exactly to the original signal, yielding Eq. (64). As PCA is also a linear transform, the subsequent projection into a 1D vector keeps the additive decomposition.

Figure 7 illustrates this construction. Panel (a) shows the wavelet coefficients of the time series displayed in panel (c). Panel (b) shows the reconstructed signals obtained from a single set of detail coefficients (d_j) at a specific scale. The original signal is recovered exactly by summing all reconstructed components across scales.

An example of what removal of high frequencies looks like in the input domain can be seen in Figure 8. The levels on top of each panel denotes the number of frequency bands that have been removed.

D Exact Values of Bounds

Table 1 contains the actual KL values, variance approximations and bounds.

E Tightness Analysis

We further investigate the accuracy of the approximation in Proposition 4 and the tightness of propositions 5 and (6).

Accuracy of Variance Approximation We first study the accuracy of the variance approximation in Proposition 4. Instead of projecting the synthetic data into a fixed 10-dimensional space, we vary

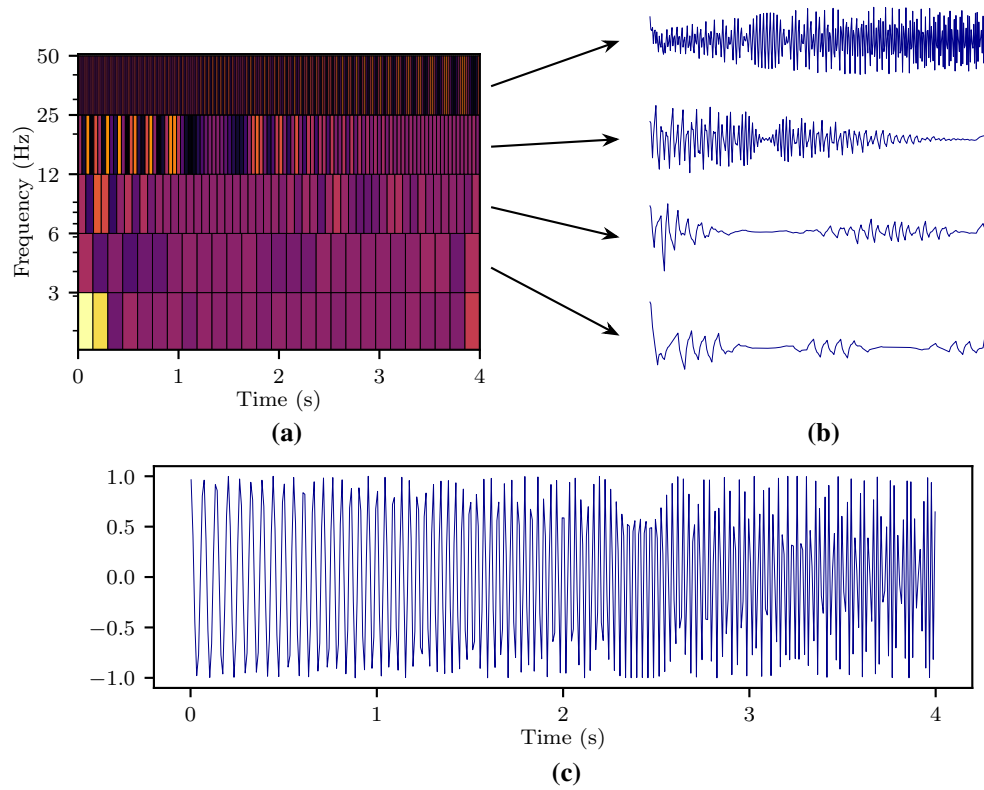


Figure 7: **(a)**: DWT of the time series seen in **(c)**. **(b)** shows the reconstructions from only a single band. This shows how the DWT ensures the additive condition in eq. (64) is satisfied.

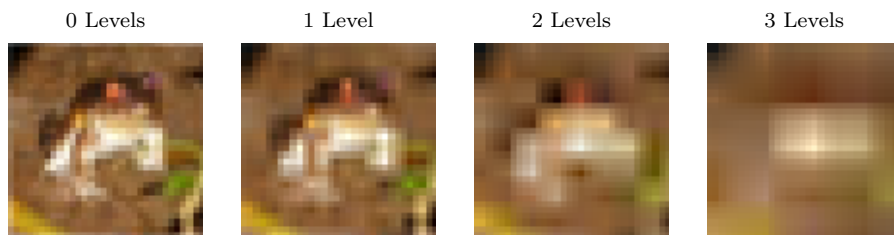


Figure 8: Illustration of the effect of removing detail coefficients content using DWT on an image. The level on top corresponds to the number of levels that have been removed in the scalogram.

Table 1: Exact values of KL-ratio, KL-diff, the variance approximation and the bounds as seen in Figure 2. Levels refer to the number of frequency bands removed in the scalogram generated from the DWT. LB = lower bound, UB = upper bound, and Cor refers to the tighter bounds in Corollary 7.

# Levels	KL Ratio	Ratio LB	Ratio UB	Ratio LB (Cor)
Levels 0	$1.0 \pm 0.00 \cdot 10^0$	$1.0 \pm 0.00 \cdot 10^0$	$1.0 \pm 0.00 \cdot 10^0$	$1.0 \pm 0.00 \cdot 10^0$
Levels 1	$1.01 \pm 1.10 \cdot 10^{-4}$	$0.95 \pm 9.00 \cdot 10^{-5}$	$1.02 \pm 9.00 \cdot 10^{-5}$	$1.00 \pm 0.00 \cdot 10^0$
Levels 2	$1.04 \pm 2.00 \cdot 10^{-4}$	$0.96 \pm 1.80 \cdot 10^{-4}$	$1.05 \pm 1.80 \cdot 10^{-4}$	$1.00 \pm 0.00 \cdot 10^0$
Levels 3	$1.13 \pm 4.30 \cdot 10^{-4}$	$0.81 \pm 8.20 \cdot 10^{-4}$	$1.21 \pm 1.01 \cdot 10^{-3}$	$1.01 \pm 9.00 \cdot 10^{-5}$
	KL Diff	Diff LB	Diff UB	Diff LB (Cor)
0	$0.00 \cdot 10^0 \pm 0.00 \cdot 10^0$	$0.00 \cdot 10^0 \pm 0.00 \cdot 10^0$	$0.00 \cdot 10^0 \pm 0.00 \cdot 10^0$	$0.00 \cdot 10^0 \pm 0.00 \cdot 10^0$
1	$1.80 \cdot 10^{-4} \pm 0.00 \cdot 10^0$	$-2.70 \cdot 10^{-4} \pm 1.00 \cdot 10^{-5}$	$2.70 \cdot 10^{-4} \pm 1.00 \cdot 10^{-5}$	$0.00 \cdot 10^0 \pm 0.00 \cdot 10^0$
2	$6.00 \cdot 10^{-4} \pm 1.00 \cdot 10^{-5}$	$-7.60 \cdot 10^{-4} \pm 1.00 \cdot 10^{-5}$	$7.80 \cdot 10^{-4} \pm 1.00 \cdot 10^{-5}$	$1.00 \cdot 10^{-5} \pm 0.00 \cdot 10^0$
3	$1.84 \cdot 10^{-3} \pm 2.00 \cdot 10^{-5}$	$-3.09 \cdot 10^{-3} \pm 6.00 \cdot 10^{-5}$	$3.40 \cdot 10^{-3} \pm 6.00 \cdot 10^{-5}$	$1.60 \cdot 10^{-4} \pm 0.00 \cdot 10^0$

the projected input dimension from 2 to 100. For each input dimension, we compute the relative error

$$e_r = \frac{\text{KL}_h / \text{KL}_l - \text{Var}[\ell(\boldsymbol{\theta}, \mathbf{x}_h)] / \text{Var}[\ell(\boldsymbol{\theta}, \mathbf{x}_l)]}{\text{KL}_h / \text{KL}_l}, \quad (65)$$

where the low-resolution input has had three wavelet bands removed. We evaluate this quantity for models with 2, 3, and 4 hidden layers. The results can be seen in Figure 9. The relative error decreases as model size increases, and remains below 3% even for the 2-layer model. This indicates that the variance approximation provides a good description of the KL-ratio.

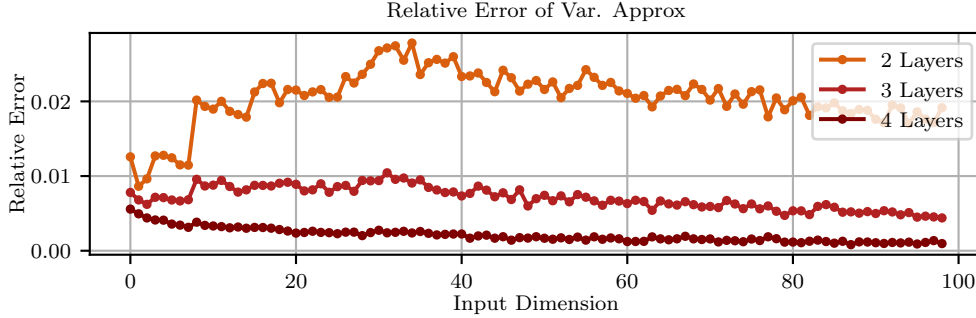


Figure 9: Relative error of the variance approximation in Proposition 4 as a function of input dimension and model size. Three levels of the scalogram are removed from the low-resolution datapoint.

Tightness of the KL-ratio bounds. To study when the bounds in Proposition 5 and Corollary 7 are tight, we define the gap between the true KL-ratio and a bound as our measure of tightness. For lower bounds, this is the difference between the true value and the bound; for upper bounds, we report the absolute difference. Figure 10 shows this analysis for projected input dimensions from 2 to 100 and for networks with 2, 3, and 4 hidden layers.

In the top panels, three wavelet bands are removed and the resulting gap is plotted as a function of input dimension. The corresponding low-resolution loss variance σ_l^2 is overlaid, since it appears in all KL-ratio bounds. In the bottom panels, we fix a 2-layer network and vary the number of removed frequency bands. The bars show the corresponding bound gaps, while the directional residual norm $\|\mathbf{x}_r\|_{\Sigma_g}$ is shown on the secondary axis. The results show that the bounds become looser as more residual information is removed, and tighter as model size increases.

Tightness of the KL-difference bounds. Figure 11 reports the analogous analysis for the KL-difference bounds in Proposition 6 and Corollary 7. The setup mirrors that of Figure 11: the top panels vary the projected input dimension for 2-, 3-, and 4-layer networks after removing three wavelet bands, while the bottom panels fix a 2-layer network and vary the number of removed bands.

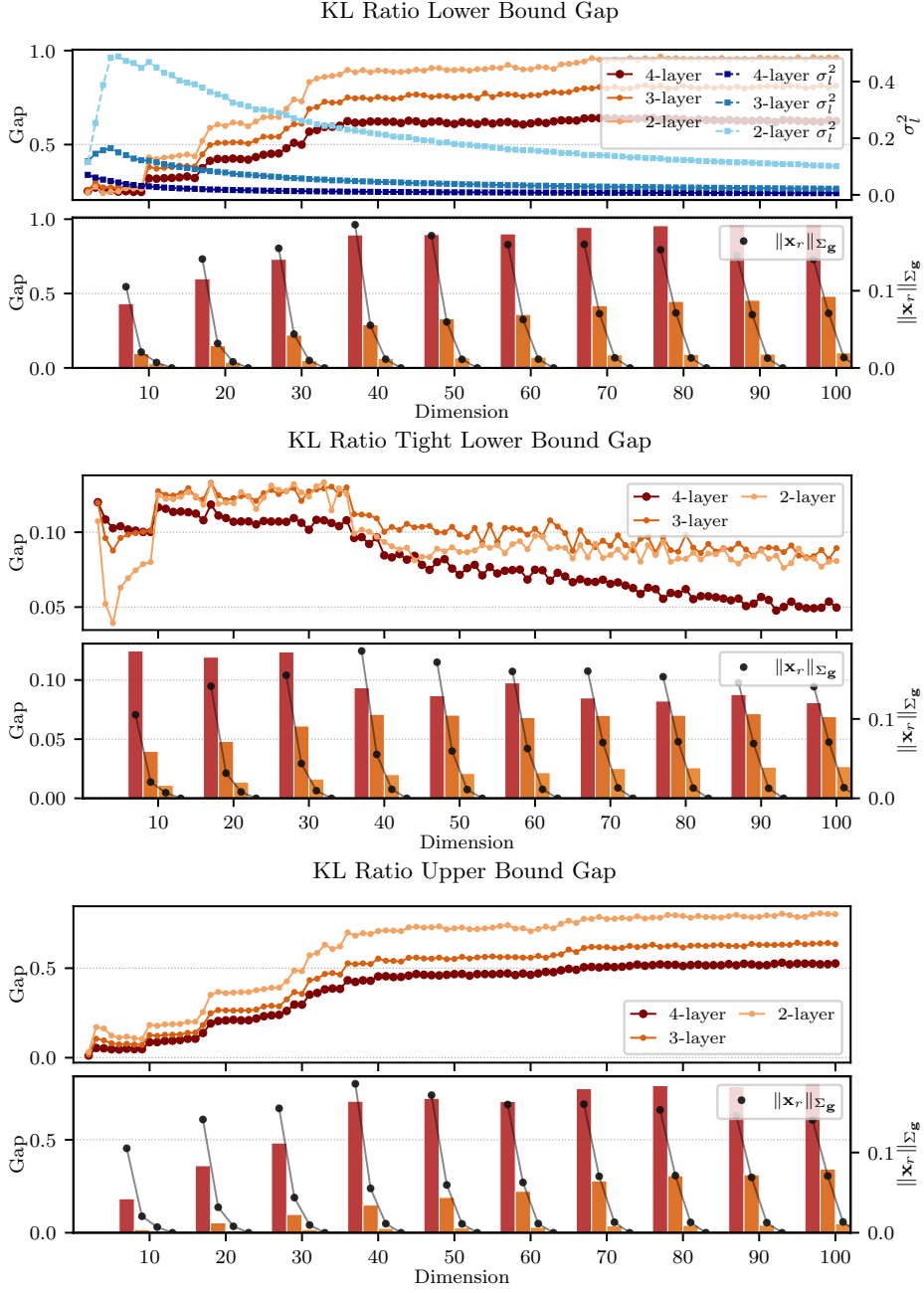


Figure 10: Tightness of the KL-ratio bounds from Proposition (5) and Corollary 7 under varying projected input dimension and removed frequency content. Top panels: gap between the true KL-ratio and each bound for 2-, 3-, and 4-layer networks after removing three wavelet bands. Bottom panels: corresponding bound gaps for a 2-layer model under different levels of removed frequency content, with the four bars representing, from left to right, the removal of three, two, one, and zero bands. The directional residual norm $\|x_r\|_{\Sigma_g}$ is overlaid on the secondary axis. The bounds become looser as more residual energy is removed

As in the KL-ratio case, the bounds become looser as the residual component grows. Overall, these results support the interpretation that the quality of the bounds is primarily governed by the magnitude of the residual information and improves for larger models.

F Training Schedule and Ablation Studies

We process minibatches proportionally to the data mixture: i.e. if the high-resolution ratio is 80%, four high-resolution batches are processed for every low-resolution batch. Training uses the AdamW optimiser with constant weight decay of 0.05, an initial learning rate of 5×10^{-4} , and a learning-rate schedule consisting of 20 warm-up epochs followed by cosine annealing. Experiments run for 100 epochs in total. Gradients are clipped to a maximum norm of 1.0. Experiments on CIFAR are run with a batchsize of 128, and 64 for AudioMNIST.

Data augmentation for the CIFAR datasets consists of random crops, horizontal flips, random erasing, and colour jitter. For AudioMNIST, we use random time shifts, random erasing, and magnitude warping. For both datasets, CutMix and Mixup are applied with probability 0.5, except for low-resolutions sizes that constitute less than 10% of the high-resolution size.

F.1 Weighting of Low-resolution Loss

Since evaluation is performed exclusively on high-resolution inputs, we anneal the contribution of the low-resolution branch during training while keeping the high-resolution weight fixed at $w_{\text{high}} = 1$. We consider two schedules for weighting the low-resolution loss.

1-phase Cosine Schedule Let $p = e/E \in [0, 1]$ denote the training progress at epoch e out of a total of E epochs. We compute a cosine annealing coefficient w , which is used to update the low-resolution loss weight:

$$w = \frac{1}{2} (1 + \cos(\pi p)), \quad w_{\text{low}} = \text{ratio}_{\text{low}} \cdot (0.2 + 0.8 w). \quad (66)$$

This schedule ensures that low-resolution samples initially contribute in proportion to their dataset share, after which their contribution decays smoothly to one fifth of that share.

2-phase Cosine Schedule Let $p = e/E \in [0, 1]$ denote the training progress at epoch e out of a total of E epochs.

The schedule consists of two phases with transition point $p^* = 0.7$ and floor $a = 0.05$. The low-resolution weight is defined as

$$w_{\text{low}}(p) = \text{ratio}_{\text{low}} \cdot \begin{cases} a + (1 - a) \frac{1}{2} (1 + \cos(\pi p / p^*)), & 0 \leq p \leq p^*, \\ a \frac{1}{2} (1 + \cos(\pi (p - p^*) / (1 - p^*))), & p^* < p \leq 1. \end{cases} \quad (67)$$

Thus, during the first 70% of training the low-resolution branch decays smoothly from its data-proportional value $\text{ratio}_{\text{low}}$ to a small floor $a \cdot \text{ratio}_{\text{low}}$, after which it is annealed continuously to zero over the remaining 30%. This yields a smooth transition from joint mixed-resolution training to pure high-resolution fine-tuning.

To account for different numbers of high- and low-resolution mini-batches per epoch, we rescale both branch weights as

$$w_{\text{low}} \leftarrow w_{\text{low}} \cdot \frac{0.5}{n_{\text{low}} / (n_{\text{low}} + n_{\text{high}})}, \quad w_{\text{high}} \leftarrow w_{\text{high}} \cdot \frac{0.5}{n_{\text{high}} / (n_{\text{low}} + n_{\text{high}})} \quad (68)$$

where n_{low} and n_{high} denote the numbers of low- and high-resolution mini-batches per epoch.

All experiments on CIFAR-100 use the 1-phase cosine schedule. On CIFAR-10 and AudioMNIST, CNN-based models performed better under the 2-phase schedule, whereas ViT-based models continued to use the 1-phase schedule.

Table 2 shows an ablation study on the CIFAR10 dataset on selected Ratio experiments. The schedule is compared to weighting the high- and low-resolution loss equally at a value of 1. The proposed schedules especially make a difference for the lower ratios. For ratios of 70% or 90%, high-resolution data already dominates and it thus matters less what the weighting of low-resolution loss is.

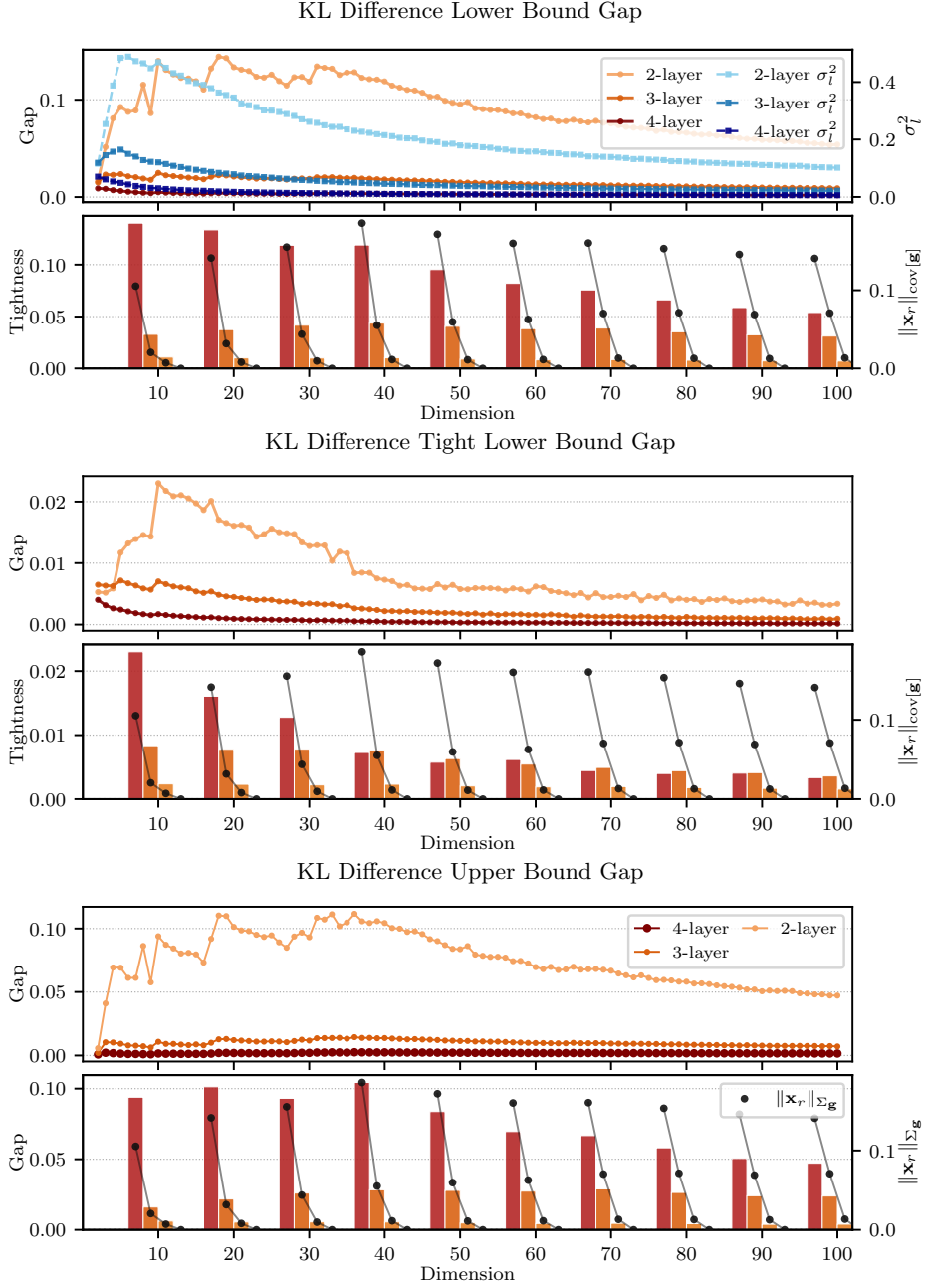


Figure 11: Tightness of the KL-difference bounds from Proposition (6) and Corollary 7 under varying projected input dimension and removed frequency content. Top panels: gap between the true KL-ratio and each bound for 2-, 3-, and 4-layer networks after removing three wavelet bands. Bottom panels: corresponding bound gaps for a 2-layer model under different levels of removed frequency content, with the four bars representing, from left to right, the removal of three, two, one, and zero bands. The directional residual norm $\|x_r\|_{\Sigma_g}$ is overlaid on the secondary axis. The bounds become looser as more residual energy is removed

Table 2: Ablation study on the low-resolution weighting for selected ratio experiments on the CIFAR10 dataset. Orig for ViT refers to the schedule in eq. (66) and for CNN it refers to eq. (67). Equal weighting means both high- and low-resolution losses are weighted with 1. "Ours" refer to the results seen in Figure 4.

Ratio	ViT		CNN	
	Ours	Equal Weighting	Ours	Equal Weighting
10%	73.4 ± 0.6	69.2 ± 0.8	77.5 ± 0.9	75.1 ± 0.7
30%	81.5 ± 0.3	78.9 ± 0.6	87.9 ± 0.4	87.1 ± 0.4
50%	85.2 ± 0.4	84.4 ± 0.3	91.4 ± 0.3	90.9 ± 0.4
70%	87.3 ± 0.2	87.3 ± 0.5	93.0 ± 0.2	92.8 ± 0.1
90%	89.2 ± 0.3	89.1 ± 0.4	93.8 ± 0.2	93.8 ± 0.1

F.2 Scale Consistency Loss

Tian et al. [2023] propose a scale-consistency loss to encourage representations learned at different input resolutions to be aligned during training. Concretely, the scale-consistency loss is defined as a smooth- l_1 loss applied to whitened feature representations. For ViTs, this loss operates on the `cls`-tokens corresponding to different resolutions:

$$\mathcal{L}_{\text{scale}} = \sum_{i=1}^{r-1} \mathcal{L}_{\ell_1}(\text{cls}_{i+1}, \text{cls}_i), \quad (69)$$

where r denotes the number of resolutions used during training, and the sum enforces consistency between adjacent resolution levels, with higher resolutions acting as teachers for lower ones. To assess whether this auxiliary loss is beneficial in our setting, we construct paired high- and low-resolution inputs by first performing a forward pass on the high-resolution samples, then downsampling these samples and passing them through the model again. This yields aligned representations at the two resolutions, to which the scale-consistency loss can be applied. We incorporate this into the loss function for selected Ratio experiments with a weighting coefficient of 0.5. For CNN architectures, the loss is computed analogously using the post-pooled feature vectors, ensuring comparability across model classes. The results are listed in Table 3. For both architectures the addition of this auxiliary loss does not yield any significant improvements.

Table 3: Ablation study on the scale consistency loss proposed by Tian et al. [2023] on selected Ratio experiments on the CIFAR10 dataset. Loss is added with a coefficient of 0.5 and applied to the `cls`-token for the ViT experiments and the post-pooled feature vector for the CNN experiments. "Ours" refer to the results seen in Figure 4.

Ratio	ViT		CNN	
	Ours	W. Scale Consistency	Ours	With Scale Consistency
10%	73.4 ± 0.6	71.0 ± 0.5	77.5 ± 0.9	77.7 ± 0.7
30%	81.5 ± 0.3	79.6 ± 0.5	87.9 ± 0.4	87.9 ± 0.2
50%	85.2 ± 0.4	84.1 ± 0.8	91.4 ± 0.3	91.3 ± 0.3
70%	87.3 ± 0.2	87.3 ± 0.4	93.0 ± 0.2	92.9 ± 0.1
90%	89.2 ± 0.3	89.3 ± 0.4	93.8 ± 0.2	93.9 ± 0.1